Monitoring and characterization of milk fouling on stainless steel using high-pressure high-temperature quartz crystal microbalance with dissipation

AUTHORS

Holly A. Huellemeier[a*], Necla M. Eren[ab*], Taylor D. Payne[c], Zachary D. Schultz[c], Dennis R. Heldman[ad]

AUTHOR AFFILIATIONS

[a]The Ohio State University, Department of Food, Agricultural, and Biological Engineering, 590 Woody Hayes Drive, Columbus, Ohio 43210

[b]Abbott Laboratories, Abbott Nutrition Research and Development, Columbus, Ohio, 43219

[c]The Ohio State University, Department of Chemistry and Biochemistry, 100 West 18th Ave, Columbus, OH 43210

[d]The Ohio State University, Department of Food Science and Technology, 2015 Fyffe Road, Columbus, Ohio 43210

*Corresponding authors' emails: Holly A. Huellemeier (huellemeier.1@osu.edu), Necla M. Eren (necla.eren@abbott.com)

KEYWORDS:

Residence time, computational fluid dynamics, clean-in-place, ultra-high temperature, stainless steel

ABSTRACT

Fouling at interfaces deteriorates the efficiency and hygiene of processes within numerous industrial sectors, including the oil and gas, biomedical device, and food industries. In the food industry, the adhesion of a complex food matrix to a heated stainless-steel surface reduces production efficiency by increasing heating resistance, pumping requirements, and the frequency of cleaning operations.

In this work, quartz crystal microbalance with dissipation (QCM-D) was used to study the interface formed by the fouling of milk on a stainless-steel surface at different flow rates and protein concentrations at high temperatures (135 °C). Subsequently, the QCM-D response was recorded during cleaning of the foulant. Two-phases of fouling were identified. During Phase-1, the fouling rate was dependent on flow rate, while the fouling rate during Phase-2 was dependent on flow rate and protein concentration. During cleaning, foulants deposited at the higher flow rate swelled more than foulants deposited at the lower flow rate. The composition of the fouling deposits consisted of both protein and mineral species. Two crystalline phases of calcium phosphate, β-tricalcium phosphate and hydroxyapatite, were identified at both flow rates. Stratification in topography was observed across the surface of the QCM-D sensor with a brittle and cracked structure for deposits formed at 0.2 mL/min, and a smooth and close-packed structure for deposits formed at 0.1 mL/min. These stratifications in composition and topography were correlated to differences in reaction time and flow dynamics at the different flow rates.

This high-temperature application of QCM-D to complex food systems illuminates the initial interaction between proteins and minerals and a stainless-steel surface, that might otherwise be undetectable in low-temperature applications of QCM-D or at larger bench and industrial scales. The methods and results presented here have implications for optimizing processing scenarios that limit fouling formation, while also enhancing removal during cleaning.

1. Introduction

Fouling is the unwanted deposition of a product on a processing surface, and it results in production inefficiencies such as reduced heat transfer rates and increased pressure drop across heat exchangers. Complex interactions between a product's physical (i.e., viscosity) and chemical properties (i.e., composition),[1,2] processing conditions (i.e., fluid mechanics),[3,4] and the processing surface (i.e., roughness, surface energetics),[5,6] significantly influence how a product fouls, as well as how it cleans. Cleaning, often in the form of clean-in-place (CIP) practices, is required to restore hygiene after fouling. Therefore, fouling and cleaning processes do not occur independently, rather they exist within a continuous cycle in industrial processes, and this cycle has significant economic and environmental consequences.[7,8] This emphasizes the need for more research studies that investigate *both* fouling and cleaning.[9] Better understanding of a foulant's structure, specifically its adhesive and cohesive forces,[10,11] as well as its composition, can help tailor a CIP cycle to meet the needs of a foulant, rather than a 'one-size-fits-all' CIP protocol.[12–14] Optimized and targeted cleaning methodologies have the potential to reduce water, energy, and chemical usage.

There has been significant research into the fouling of milk under pasteurization or high-temperature short-time (HTST) conditions (72 °C ≥15 s), but research is limited regarding fouling during ultra-high temperature (UHT) milk processing (130–140 °C, 1–2 s) and even further limited for the cleaning of UHT milk deposits. The prevalence of HTST fouling studies is in part due to greater ease-of-access to equipment simulating HTST processing conditions because there is no need for back-pressure to prevent product flashing, which occurs at temperatures >100 °C. Ultimately, there is a need to improve mechanistic fouling knowledge and access to bench-scale devices for UHT milk processing.

One bench-scale device that has shown promise in studying fouling is quartz crystal microbalance with dissipation (QCM-D). QCM-D relies on the piezoelectric effect in which the compression of a crystal with a specific lattice symmetry, such as AT-cut quartz, results in a voltage and vice-versa. In QCM-D, an alternating voltage is applied at the resonant frequency of a quartz crystal resulting in a standing wave. The resonant frequency of the crystal shifts with changes in the properties of the fluid (i.e., density, viscosity, etc.) or a deposit at the crystal surface. Periodically, the driving voltage is turned off and the relaxation behavior of the crystal's oscillatory motion is measured to describe energy loss or dissipation.[15] Therefore, QCM-D results in two pieces of data, frequency (ΔF) and dissipation (ΔD) shifts, which are measured relative to the fundamental frequency and at odd-multiples or overtones of the fundamental frequency. Monitoring of overtone-dependent ΔF and ΔD supports applications of QCM technology for both gravimetry and rheology.[16,17] With application to fouling, measurements of ΔF and ΔD with QCM-D can be used to measure the deposition, removal, and structure of a deposit on the sensor surface. The extreme sensitivity of QCM-D (limit of detection in liquid ≈1–2 ng/cm^2) resolves molecular interactions that would otherwise be 'invisible' to metrics of fouling measured by process instrumentation (i.e., pressure and temperature transducers).[18]

With regards to milk fouling, QCM-D has been used at elevated temperatures (≤65 °C) to understand how the composition of a model milk-based fluid affects the rate of fouling.[18,19] In addition, QCM-D has been used to monitor fouling and cleaning during the stages of a simulated pasteurization process.[20] The maximum temperature of fouling in these studies (65 °C) was constrained by instrumental limitations and did not exceed the denaturation temperature of whey proteins, such as β-lactoglobulin (≥70 °C, ~pH 6.6),[21] which has been closely linked to HTST fouling,[22–24] nor temperatures required to aggregate and coagulate casein micelles (>110 °C, ~

pH 6.5–6.7)[25] which may have an effect on UHT fouling. To overcome this temperature limitation in this study, a high-pressure high-temperature (HPHT) attachment for QCM-D (QSense High Pressure, Biolin Scientific, Gothenburg, Sweden) with the capability of achieving temperatures and pressures up to 150 °C and 250 bar, respectively, was adapted to study biological samples at high temperatures (>100 °C) with advanced controls at low pressures (~10–15 bar) which is critical for industrial applications such as UHT and HTST milk processing.

Application of QCM-D technology in the oil and gas industry, where QCM-D technology has been used to investigate the use of additives to inhibit asphaltene deposition, has laid the foundation for the application of HPHT QCM-D to study fouling in biological applications. Asphaltene is one of the densest functional molecules in crude oil and, analogous to proteins in food systems, is easily destabilized due to environmental conditions (i.e. temperature, pressure, presence of solvent, etc.).[26] High-temperature QCM-D,[26–28] and even HPHT QCM-D,[29,30] have been applied to study how surface composition, flow rate, asphaltene stability, asphaltene polydispersity, and presence/absence of an inhibitor effect asphaltene deposition or fouling.

In this study, fouling of a milk-based model fluid, and its subsequent removal during clean-in-place was monitored *in-situ* using HPHT QCM-D. The fouling layers after the water-rinse cleaning step, namely the irreversible foulants, were characterized using physical and chemical methods. The specific objectives of this study included: (1) explore the limits of HPHT QCM-D in the UHT fouling of a complex milk-based fluid and the subsequent cleaning of the foulant during clean-in-place, (2) investigate the role of chemical reactions vs. mass transport during fouling at nano- and micro-scales, and (3) characterize the irreversible foulant formed on a stainless-steel food-contact surface to gain a better understanding of its removal during cleaning.

2. Materials and Methods

2.1 *Sample preparation*

Milk protein concentrate (MPC 85, Milk Specialties, Eden Prairie, MN) with a protein content of 85.8% was used to create two model fouling fluids with protein concentrations of 17.5 g/L and 35 g/L. Phosphate buffered saline (1X PBS, Sigma Aldrich, St. Louis, MO) solution was used as a buffer fluid (0.01 M phosphate buffer, 0.154 M NaCl, pH 7.4). Batches of 100 g were hydrated at 50 ± 2 °C with light agitation for 1 hour. Samples were subsequently homogenized (~50 °C) using a high-shear, bench-top homogenizer (PowerGen 500, Fisher Scientific, Waltham, MA) for 10 min at 6 500 RPM. Without pH adjustment, the 35 g/L sample had a pH of 6.76 ± 0.02 (~25 °C), whereas the 17.5 g/L sample had a pH of 6.88 ± 0.02 (~25 °C). To minimize any effect of pH on fouling behavior, the 17.5 g/L sample was titrated at ~25 °C with 1 M HCl to a pH of 6.76 ± 0.02. Solutions were stored overnight (~12 hr) at 4 °C. On the day of experimentation, the pH was verified, and solutions were degassed prior to loading into the sample cylinder. Additional compositional details for the MPC 85 powder can be found in the Supporting Information (SI) (Tables S1-S2).

2.2 *HPHT QCM-D experiments*

2.2.1 Stainless-steel sensor preparation

Stainless steel (SS) coated QCM-D sensors (QSX 304, Nanoscience Instruments, Phoenix, AZ) with a resonant or fundamental frequency of 4.95 MHz were cleaned according to the manufacturer's instructions by soaking in 1% v/v Hellamanex II solution overnight (~12 hr), rinsing with MilliQ water, sonicating in 100% EtOH for 10 mins, rinsing in MilliQ water, drying with purified N_2 gas, and exposing to an ozone/UV treatment for 10 mins.

2.2.2 HPHT QCM-D instrumentation

A process and instrumentation diagram (PID) for the QSense HPHT QCM-D equipment can be found in Figure 1. A picture of the physical instrument, highlighting key components found in this PID, can be found in the SI (Figure S1).

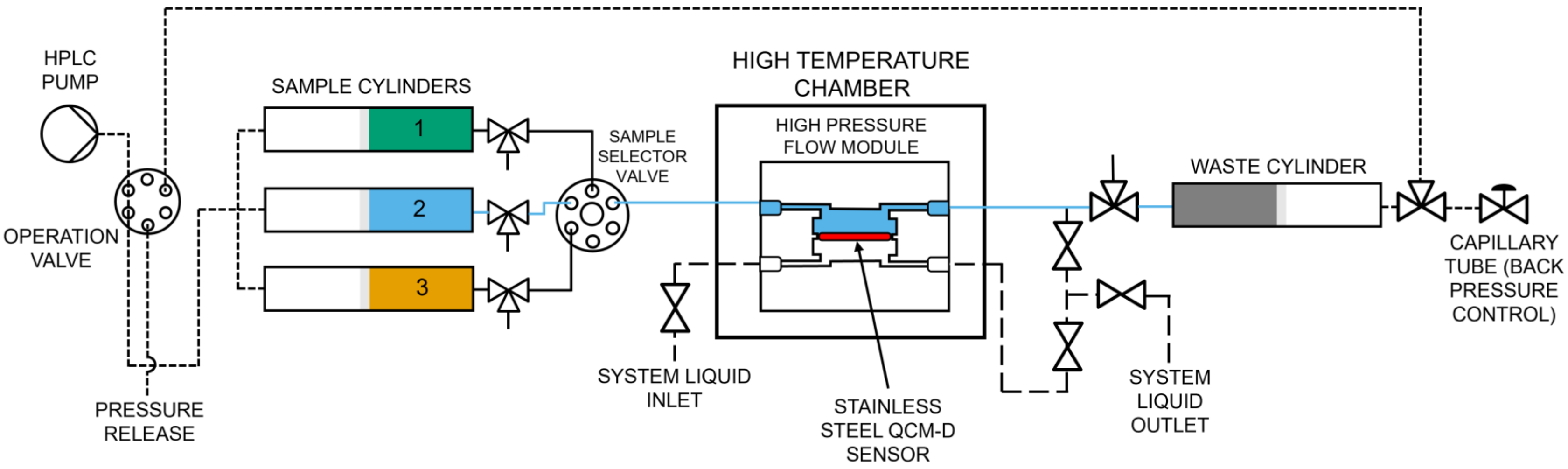

Figure 1. Process and instrumentation diagram (PID) for QSense high-pressure high-temperature quartz crystal microbalance with dissipation (HPHT QCM-D). The system consists of three sample cylinders reserved for (1) sample, (2) MilliQ water, and (3) 0.1 M NaOH. Three flow paths are highlighted: (1) the flow path for sample cylinder #2 (MilliQ water) is highlighted in blue, (2) the short-dashed line (---) indicates the flow path for the driving fluid (MilliQ water), and (3) the long-dashed line (– –) at the bottom of the flow chamber indicates the flow path of the system liquid. The location of the stainless-steel quartz sensor is highlighted in red. Reproduced with permission from Biolin Scientific.

Degassed MilliQ water, the ‘driving liquid’, was used to pressurize and push sample out of the sample cylinders. The HPHT QCM-D instrument only has three sample cylinders which limits the number of samples used during an experiment. In these experiments, the three cylinders were dedicated to MPC solution, MilliQ water, and 0.1 M NaOH. The ‘system liquid’, was filled on the backside of the sensor to ensure pressure equalization on the top and bottom of the sensor such that there is no bowing or cracking of the sensor under high-pressures. The back pressure was held constant at 12.3 ± 0.3 bar during each experiment. This pressure was selected not only to prevent flashing at temperatures >100 °C, but also to prevent pressure fluctuations during experimentation.

Heat was supplied from two sources: (1) an external hot plate set at 15 °C below the target temperature (120 °C for these experiments) and (2) a fine-tuning Peltier element within the high-temperature chamber which was set at the target temperature (135 °C). The system was preheated for 1.3–1.5 hours, which was the time required to achieve a stable temperature at 135 °C as recorded by the data acquisition software (QSoft, version 2.8.4.948, Biolin Scientific). Absolute dissipation, which is related to fluid viscosity ($\Delta D \propto \sqrt{\eta}$),[15,31] was monitored to ensure the stabilization of the temperature of the liquid near the SS sensor surface. The dissipation shift recorded during preheating (25 to 135 °C) with flowing MilliQ water for the 3rd overtone of a SS sensor and a hydrostatic pressure of ~12.3 bar was ~150E–6.

The titanium, high-pressure flow module (QHPC 101, Biolin Scientific) contains two primary flow sections, similar to those described in a previous study for the standard flow module (QFM 401, Biolin Scientific).[18] The first flow section is a ‘preheating’ section which has a total volume of 23.7 μL. In the preheating section, fluid enters the heated titanium flow module and is rapidly heated from 25 to 135 °C. The second flow section is ‘contact’ section which has a total volume of ~33–36 μL (extent of gasket compression changes volume). In the contact section, the SS sensor is exposed to the sample fluid and the fouling/cleaning response is measured.

2.2.3 HPHT QCM-D data collection

At the desired processing temperature and flow rate, the sensor was calibrated at seven odd-overtones/harmonics (n) (n = 1,3,5,7,9,11,13), which are odd multiples of the fundamental frequency (f_1 = 4.95 MHz), and a water baseline was collected for 2 mins before switching to the MPC solution. All reported frequency and dissipation shifts are normalized by the overtone number (i.e., $\Delta f_3 = \Delta(3 * f_1)/3$). Sample fluids were continuously passed over the SS surface as follows: (1) MPC for 20 min or until signs of over-dampening, (2) MilliQ water until stabilized (10-20 min), (3) 0.1 M NaOH (pH 12.9) for 30 min, and (4) MilliQ water for an additional 20 min. Stage 1 was run at the desired experimental flow rate (0.1 or 0.2 mL/min), while stages 2–4 were all run at 0.1 mL/min. For 35 g/L at 0.1 and 0.2 mL/min, data was collected for all experimental stages (1–4) for 3 replicates (N) (N = 3). For 17.5 g/L, fouling and water rinse data (stages 1–2) was collected for N = 4 and 2 samples were sacrificed for characterization of irreversible fouling layers, resulting in N = 2 for fouling and cleaning data (stages 1–4). The temperature was kept constant at 135.0 ± 0.2 °C during all fouling and cleaning stages.

2.3 Irreversible fouling characterization

The irreversible fouling layers formed by the 17.5 g/L solution at both flow rates (0.1 and 0.2 mL/min) were characterized using multiple methods. Samples at both flow rates were analyzed in duplicate (N = 2). Samples were air-dried at least 24-hours before characterization by 3-D laser scanning microscopy, Raman spectroscopy, and atomic force microscopy.

2.3.1 3-D laser scanning microscopy (LSM)

The topography of irreversibly bound milk deposits was characterized by 3-D LSM (VK-X200, KEYENCE, Itasca, IL). Laser height and intensity were automatically optimized, and images were captured at a magnification of 10x along the centerline of the flow path (from inlet to outlet) on the sensor surface. The centerline of the flow path is highlighted by the yellow-dashed line in the 3-D geometry used for computational fluid dynamics (#4 in Figure 2).

2.3.2 Raman spectroscopy

Raman spectroscopy was used for qualitative identification of major fouling components. Extended scan Raman spectra were collected using a Renishaw inVia Qontor microscope equipped with a 785 nm laser operating at 100 % power and spatially filtered through a pinhole to provide 5 mW of power at the sample. A 50x objective (NA = 0.50), a 1200 grooves/mm grating, and an acquisition time of 120 s were used to collect spectra at five approximately equidistant spots along the centerline (#4 in Figure 2) of the fouled SS surface. Spectra were also collected from clean SS sensors to serve as a control (N = 2). Cosmic ray removal was performed in Renishaw's Windows-based Raman Environment (WiRE) software (version 5.2.10411). MATLAB (R2019a, The Mathworks Inc., Natick, MA) was used to identify peak locations and intensities using the 'islocalmax' function.

2.3.3 Atomic force microscopy (AFM)

A Bruker Icon Dimension AFM (Bruker Corporation, Billerica, MA) was used to characterize the topography with higher resolution as compared to LSM and dry mass-thickness of the irreversible fouling layers. For both topography and thickness measurements, Bruker

NCHV-A cantilevers (k = 42 N/m, rectangular tip, radius = 8 nm) were used. For topography, surfaces were scanned at 0.5 Hz and 256 samples/line for 10 µm x 10 µm scan size in tapping mode at numerous locations across the surface along the centerline of the flow path (#4 in Figure 2). NanoScope Analysis 1.2 (Bruker Corporation) was used to calculate surface roughness and measure the particle size of fouling components. Large cracks in the foulants formed at 0.2 mL/min were avoided during roughness measurements.

For thickness measurements, an AFM nano-indentation or scratching technique was employed.[20] Using contact mode, a defined deflection force was applied to the NCHV-A cantilever resulting in a contact force of ~ 62 µN for 20 s at 1 Hz with a 90 µm scan size. This resulted in complete penetration of the foulant layer as indicated by visibility of the SS surface after 20 s of contact with the surface. Debris was removed with compressed air and a new tip was installed prior to thickness measurements. Thickness measurements were made in tapping mode for 10 µm x 10 µm scan sizes at 1 Hz and 256 samples/line at three equidistant locations spanning the centerline of the flow path. The 'Step' program option in the NanoScope Analysis software was used to quantify deposit thickness.

2.4 Modelling

2.4.1 Empirically modelling the frequency curve: bent-cable model

To describe the effects of the experimental treatments on the QCM-D response, a bent-cable model (Equation 1)[32] containing 5-parameters was fit to the frequency curve.

$$y = \beta_0 + \beta_1(x - \alpha) + \beta_2\sqrt{(x - \alpha)^2 + \gamma^2/4} \tag{1}$$

Where y is frequency [Hz] and x is time [s]. The five model parameters are β_0 [Hz], β_1 [Hz/s], α [s], β_2 [Hz/s], and γ [1, dimensionless]. MATLAB (R2019a, The Mathworks Inc.) was used to fit the bent-cable model to the frequency curve using a weighted non-linear least squares (NLLS) fitting procedure. More information regarding the weighted NLLS algorithm can be found in the SI (section S.1.3). To determine whether the treatments (flow rate and protein concentration) had a significant effect (p <0.05) on the model parameters, an ANOVA was performed using JMP Pro14 (SAS, Cary, NC) for each model parameter with discrete effects of flow rate, protein concentration, and the interaction effect of flow rate and protein concentration. Models were stepwise reduced to determine significant effects. Studentized residuals were evaluated to confirm ANOVA's assumption of normally distributed errors.

2.4.2 Computational fluid dynamics (COMSOL)

COMSOL Multiphysics ® 5.3 (COMSOL Inc., Burlington, MA) was employed to estimate the flow and pressure distribution near the sensor surface. The model was implemented in 3-D and the dimensions associated with the flow module were made available upon request from the QCM-D manufacturer (Biolin Scientific). The dimensions for the high-pressure flow module (QHPC 101, Biolin Scientific) are different than those described for the standard flow module (QFM 401, Biolin Scientific) in Huellemeier et al. (2022). The geometry and mesh are described in Figure 1 and consists of 3 key components: (#1) inlet internal borings, (#2) flow above the sensor surface, (#3) outlet internal borings. A fine, physics-controlled mesh with 132 496 elements was used (Figure 2). The system was modelled under laminar flow conditions and at steady state (stationary). The following boundary conditions were applied: (1) constant inlet velocity of 2.12E–3 or 4.24E–3 m/s for 0.1 mL/min or 0.2 mL/min, respectively, (2) constant outlet pressure of 12.5 bar, and (3) no-slip wall condition at all other boundaries.

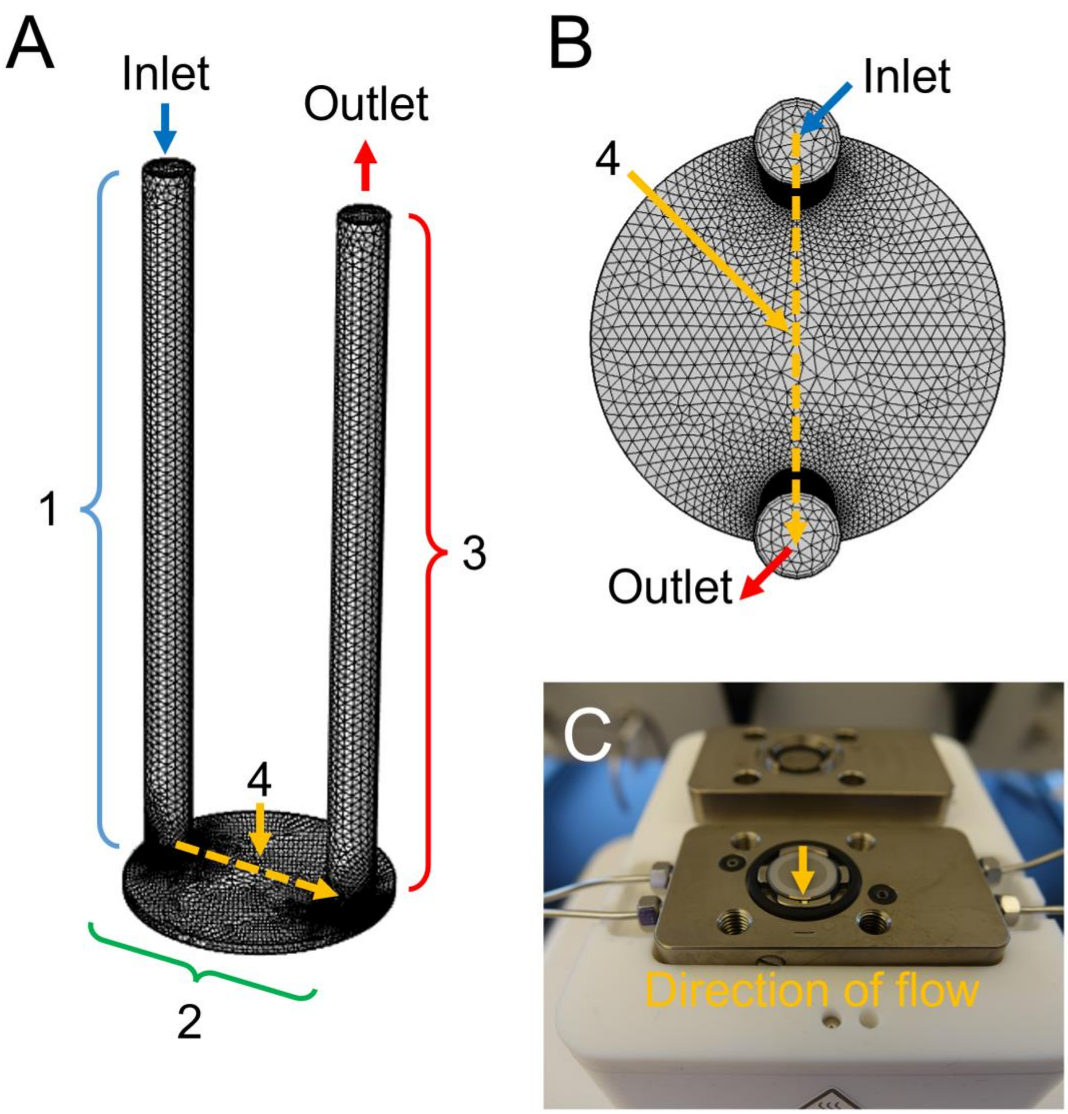

Figure 2. 3-D geometry and mesh implemented in COMSOL. (A) Isometric view highlighting 4 key features: (1) inlet tubing (blue), (2) sensor flow chamber (green), (3) outlet tubing (red), and (4) centerline of flow (yellow). The inlet and outlet flow paths are highlighted with arrows and labelled in blue and red, respectively; (B) Top view of geometry showing location of inlet and outlet as well as (4) the centerline of flow which extends from the center of the inlet to the center of the outlet. All dimensions were supplied by Biolin Scientific (Biolin Scientific); (C) physical picture of open QSense High-Pressure flow module with stainless-steel sensor surface exposed and direction of flow highlighted in yellow.

Velocity, pressure, and residence time profiles were extracted along a cut plane located at half-height of the flow chamber above the sensor surface (Figure S3A) and along the centerline of flow on this cut plane (#4 in Figure 2, Figure S3B). In an industrial milk processing system, a thermal process is defined by a specific time-temperature combination (i.e., 15 s at 72 °C for high-temperature short-time pasteurization) needed to produce a substantial logarithmic reduction in the population of a harmful microorganism. This thermal treatment generally occurs within a hold tube where the length and flow rate of the tube are defined to achieve the desired thermal treatment. The average time it takes for fluid to travel from the beginning of the hold tube to the end of the hold tube is commonly referred to as the 'hold time' or 'residence time'. In this paper, we refer to this time as the *total* residence time. In comparison, *local* residence time is defined as the amount of time fluid that has been heated at a specific location within the hold tube. The local residence time (τ_L) is a function of location and velocity, whereas the total residence time (τ_T) is a function of total volume and volumetric flow rate (or average velocity and distance in a cylindrical pipe).

Total residence (τ_T) time is defined as,

$$\tau_T = \frac{1}{\dot{Q}}(V_{inlet} + V_{sensor}) \tag{2}$$

Where $\dot{Q}$ is the volumetric flow rate (0.1 or 0.2 mL/min in this study), V_{inlet} is the volume of the inlet tubing (~24 uL, #1 in Figure 2A), and V_{sensor} (~33 uL, #2 in Figure 2A, exact volume depends on extent of gasket compression) is the active flow volume above the sensor surface. The total residence times at 0.1 and 0.2 mL/min are ~34 and 17 s, respectively.

In addition to total residence time, local residence time (τ_L) along the cut plane at half-height above the sensor surface (Figure S3A) was estimated as,

$$\tau_L(x,y,z,v) = \tau_{T,inlet} + \tau_{L,sensor}\,(x,y,z,v) \tag{3}$$

Where $\tau_{T,inlet}$ is the residence time spent in the inlet tubing and $\tau_{L,sensor}$ is the local residence time along the center cut plane in the sensor chamber. In Eq. 3, $\tau_{T,inlet}$ is a constant value and defined as $V_{inlet}/\dot{Q}$ from Eq. 2. Therefore, $\tau_{T,inlet}$ contributes an additive effect to local residence time. The come-up time, or the time required for the fluid temperature to reach the temperature of the surrounding titanium flow module from ambient conditions (25 to 135 °C), is assumed to be negligible given the volume of the chamber << volume of the inlet internal borings and due to the high thermal conductivity of titanium.[18]

In contrast, $\tau_{L,sensor}$ is a function of location along the center plane and the magnitude of local velocity from the 3D model and is estimated as

$$\tau_{L,sensor}\,(x,y,z,v) = \frac{d}{v_{xyz}} \tag{4}$$

Where v_{xyz} is the magnitude of the average velocity at a specific location (x,y,z) on the cut plane, and d is the distance from the center of the inlet calculated as,

$$d = \sqrt{(x_{ci} - x)^2 + (y_{ci} - y)^2} \tag{5}$$

Using these expressions, the total residence time and local residence time along the center cut plane within the high-pressure QCM-D flow module can be estimated.

3. Results and Discussion

3.1 Monitoring fouling and cleaning with HPHT QCM-D

3.1.1 Frequency and dissipation shifts during fouling

Frequency (ΔF) and dissipation (ΔD) shifts were collected using HPHT QCM-D during UHT fouling (Figure 3A-B) for MPC solutions at two different protein concentrations and flow rates. The 17.5 g/L sample fouled at 0.2 mL/min proved to be the most unstable sample with over-dampening for some samples occurring as early as ~15 min; therefore, the average frequency and dissipation curves for only the first 800 s of fouling are shown for all replicates. The frequency and dissipation curves for all replicates during fouling can be found in the SI (Figure S4).

The results show a considerable frequency drop (several thousand Hz) and dissipation rise during fouling. Frequency shifts of this magnitude occurred 3–12X faster in this study than those reported for an acidic whey protein solution fouled at 65 °C using QCM-D.[18]

The frequency curve (Figure 3A) demonstrates a two-phase fouling mechanism:

1. Phase-1: a mixture of non-linear and linear, *slow* fouling occurring at times < ~600s and measuring < ~500 Hz.
2. Phase-2: linear, *fast* fouling occurring at times > ~600s resulting frequency shifts > ~500 Hz

This two-phase behavior was observed in all samples with the most reproducibility in the early stages of Phase-1 (inset graphs, Figure 3A) and greater variability in Phase-2, especially in the transition timepoint between Phase-1 and Phase-2. In addition, lower flow rate treatments were more reproducible than higher flow rate treatments (Figure S4).

The discrimination of these two phases of fouling is further illuminated by ΔD vs. ΔF plots (Figure 3C) which describe the fouling curve irrespectively of time. This curve can be used to describe differences in the conformation of molecules, especially proteins, at the surface[33] and, in the case of complex samples such as milk, this curve may be indicative of a different chemical composition within each fouling phase. For all concentrations, during increasing negative frequency shift or fouling, there is a rapid rise in dissipation during Phase-1, as opposed to a much more gradual change in dissipation during Phase-2. This may suggest a difference in composition between the foulant formed during Phase-1 and Phase-2, such as the initial deposition of protein, followed by the deposition of calcium phosphate precipitates,[34] but further work is needed to discriminate the chemical composition within each phase.

This two-phase fouling mechanism may be consistent with the two-phases of fouling, 'induction/lag-period' and 'fouling/growth' periods, observed in other, larger scale fouling studies. On an industrial or pilot scale, the induction or lag-period consists of negligible or undetectable changes in processing efficiency due to fouling. Whereas, during the second phase of the fouling or growth period, fouling is measurable by process instrumentation, resulting in quantifiable processing inefficiencies (i.e., increases in pressure drop and heating resistance).[35]

This differentiation in the phases of UHT milk fouling described by HPHT QCM-D can be compared with other studies which employ bench-scale methods of fouling detection. Recent studies that monitored the fouling (145 °C) of milk protein solutions through changes in overall heat transfer coefficient (OHTC), observed a 'surface conditioning' phase (duration ≤10 min) within a longer induction phase (duration ≤30–90 min) prior to the fouling/growth phase.[36] In comparison, during the UHT processing of skim and whole milks (140 °C) in a continuously stirred vessel, multiple phases of fouling, quantified by changes in thickness and mass after defined heat times, were not observed; albeit, methods in this study did not offer real-time measurements of fouling, and data was not presented for early time points (<15 min).[37]

Compared to the findings of these previous studies,[36,37] the present study illustrates how multi-scale investigations illuminate different aspects of fouling through increasing sensitivity with decreasing scale. During Phase-1, QCM-D describes an induction-phase which features slow fouling, but rapid changes in viscoelasticity. During Phase-2, QCM-D describes a fouling period with a constant-rate in terms of frequency shift. This constant-rate trend is consistent with larger scale UHT milk fouling experiments.[37] Differences in the duration or presence of an induction phase on larger scales [36,37] compared to the measurements of QCM-D are likely due to surface-bulk fluid temperature differentials and enhanced mass transfer with turbulent flow conditions encountered on larger scales.

The significance of the dissipation shift ($\Delta D > 0$) in all samples (Figure 3B) may be indicative of viscoelasticity in the deposits. But this dissipation should be considered in the context of the frequency shift by calculating the acoustic ratio ($\Delta D/\Delta F$). During fouling in these experiments, the acoustic ratio is always less than 4E–7 Hz^{-1} which is the threshold for laterally homogeneous, Sauerbrey layer (albeit, the ratio should be << 4E–7).[15] In addition, there was little deviation between overtones for frequency and dissipation shifts which is indicative of a rigid foulant (SI, Figure S5). This indicates the Sauerbrey model[38] may be useful in estimating the areal mass density (mg/m^2) especially at long times (t = 800 s) where the acoustic ratio has a magnitude of 1E–8 (SI, Figure S6, Table S3). The Sauerbrey model linearly relates areal mass density (Δm) to overtone normalized frequency shift ($\Delta f/n$) by $\Delta m = -(C \cdot \Delta f)/n$, where C is the mass sensitivity constant which depends on properties of the quartz resonator (C = 0.180 mg Hz^{-1} m^{-2} for the sensors used in this study).[39] Sauerbrey estimates of mass density include all mass coupled to the sensor surface, which includes contributions of trapped water within a deposit on the sensor surface.[40,41] Application of the Sauerbrey equation to a viscoelastic deposit, where viscosity dominates elasticity, typically leads to an underestimation of the adsorbed mass or deposit thickness.[42]

Viscoelasticity is also represented by the deviation in frequency and dissipation shifts between different overtones/harmonics (n). The standard deviation of the frequency and dissipation shifts between the 5th, 7th, and 9th overtones fluctuates during the fouling period (SI, Figure S7). Generally, the deviation increases and then decreases near the transition point between Phase-1 and Phase-2 fouling. This further supports the use of the Sauerbrey model in estimating areal mass density, especially during Phase-2.

3.1.2 Frequency and dissipation shifts during cleaning

After fouling, three cleaning steps were performed: MilliQ water pre-rinse until stabilized (10–20 mins), 0.1 M NaOH for 30 mins, and MilliQ water mid-rinse for 20 mins, all at 0.1 mL/min. This clean-in-place (CIP) protocol was designed to mimic the first three steps of a traditional 5-step CIP applied in the dairy industry: (1) pre-rinse with water, (2) alkali wash to remove organic residues (i.e., proteins), (3) mid-rinse with water, (4) acid cleaning to remove inorganic residues (i.e., minerals), and (5) final rinse with water. Steps 1–3 were selected for study because these are often performed at elevated temperatures in industry. There are limited studies which apply an alkali cleaner such as NaOH at temperatures >100 °C,[43] but these cleaning temperatures are industrially relevant for sterilize- or steam-in-place (SIP) protocols (generally ≥121 °C).[44] The ability to measure the cleaning response at temperatures different than the processing temperature for QCM-D studies is limited due to the inherent temperature-dependence of the frequency and dissipation responses.[16,45] In addition, this study features laminar flow conditions whereas most cleaning scenarios encountered in industry are apply turbulent flow. The laminar flow conditions in this study (Re <4) are expected to isolate the chemical reactions and diffusive mass transport associated with cleaning, compared to the additional physical forces associated with turbulent flow, such as wall shear stress and convective mass transport.

Alkaline cleaners, such as NaOH, result in the dissolution of proteinaceous material within a foulant. This dissolution is due to the breakage of covalent bonds, such as intermolecular disulfide bonds,[46] and non-covalent interactions, such as hydrogen-bonds, hydrophobic interactions, and intermolecular β-sheets.[47,48] Dissolution is aided by swelling which is an increase in the void fraction of a foulant matrix.[49] Swelling and dissolution of whey protein gels upon exposure to NaOH has been extensively studied.[50,51]

During this study, cleaning information could not be recorded for all samples due to instrumental limits. Foulants formed at 0.2 mL/min, both from 17.5 and 35 g/L, demonstrated immense swelling, as evidenced by the rapid dissipation rise, when exposed to 0.1 M NaOH. Swelling of these deposits resulted in over-dampening of the quartz resonator and data from all overtones was lost. Furthermore, one replicate of the 35 g/L at 0.2 mL/min demonstrated over-dampening at the start of the water rinse period. With the loss of data during over-dampening, the electronics unit recalibrated the sensor, but this resulted in a new baseline (~0 Hz) at an unknown level of cleanliness/dirtiness; this behavior is illustrated in Figures S8, S10, and S12. Therefore, cleaning data from these samples could not be analyzed, but the immense swelling behavior was demonstrated by at least two replicates fouled at 0.2 mL/min, for both 17.5 and 35 g/L. This suggested that fouling formed at 0.2 mL/min (shorter residence time) may have had a higher concentration of protein or a structure more conducive to diffusion of NaOH than fouling formed at 0.1 mL/min (longer residence time).

The cleaning process for foulants formed by 17.5 and 35 g/L at 0.1 mL/min is illustrated in Figure 3D. Additional cleaning data for replicates of these treatments can be found in Figures S9 and S11. During the water pre-rinse, reversibly bound deposits are removed, and the viscosity of the bulk fluid decreases with the transition of sample to water. The frequency curve demonstrates that a substantial amount of the deposit is irreversibly bound because there is little positive frequency shift which would be indicative of a removal of mass. This was also the case for most deposits formed at 0.2 mL/min (Figures S10 and S12).

The addition of 0.1 M NaOH resulted in swelling as evidenced by a small decrease in frequency and rapid rise in dissipation. This swelling behavior is indicative of proteinaceous material within the fouling matrix. This observation of swelling is in contrast to previous studies which were unable to observe swelling, macroscopically, while cleaning UHT foulants.[43] A significant amount of deposit remains after exposure to 0.1 M NaOH for 30 mins for deposits formed at 0.1 mL/min. Based on removal of organic matter by NaOH, the remaining deposit likely contains inorganic matter, such as mineral species. Therefore, this remaining deposit would be expected to be removed by an acid cleaning step, but this cleaning step occurs at much lower temperatures than those applied in this study.

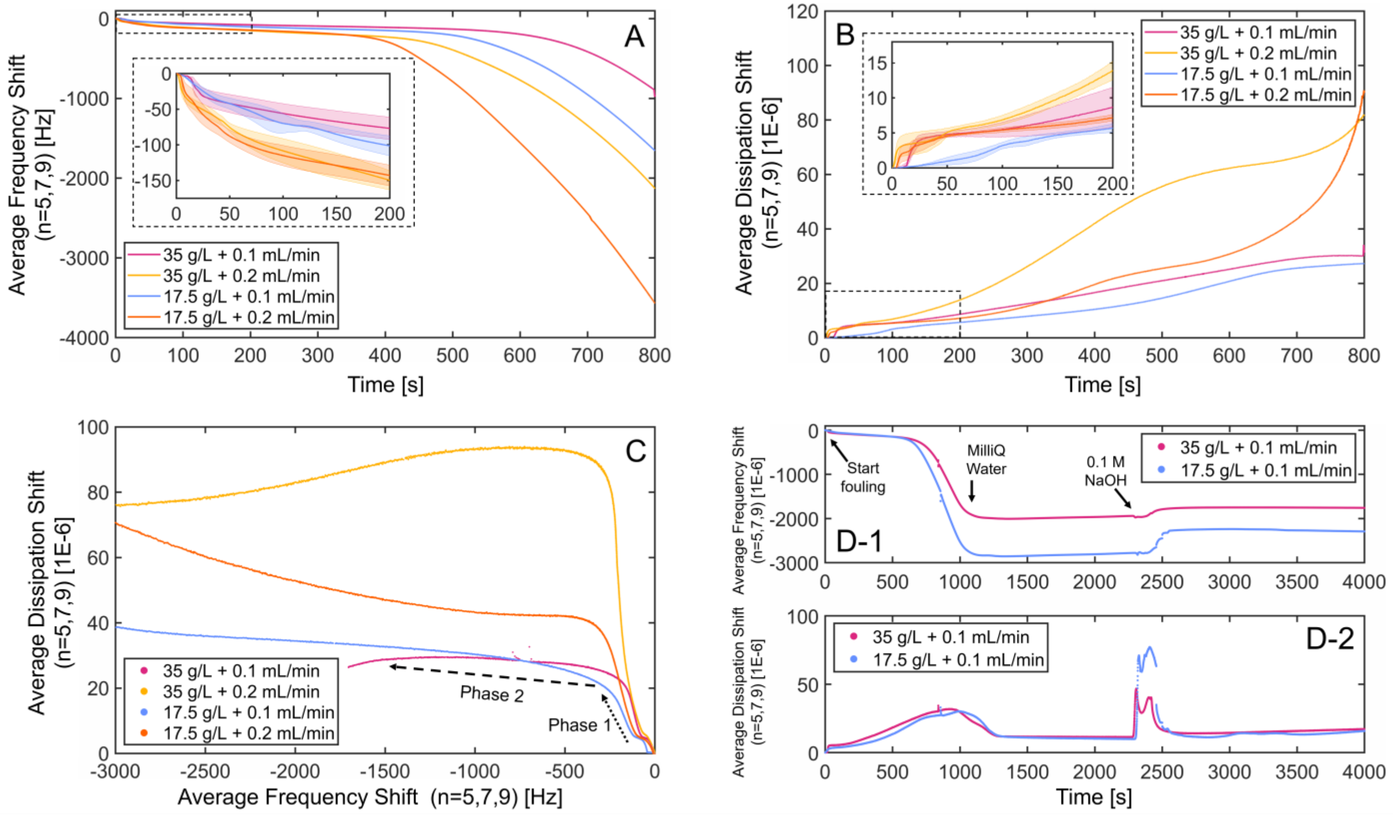

Figure 3. Shifts in frequency and dissipation during fouling and cleaning for fouling at 35 and 17.5 g/L and flow rates of 0.1 and 0.2 mL/min at 135 °C. (A) Shifts in frequency and (B) dissipation and during first 800 s of fouling period. Curves represent the average of frequency and dissipation shifts for the 5th, 7th, and 9th overtones of N = 3 for 35 g/L and N = 4 for 17.5 g/L formed at different flow rates (0.1 and 0.2 mL/min). The shaded region in the inset graphs (first 200s of fouling) describes the SEM. See SI for frequency and dissipation curves during fouling for all replicates (Figure S4); (C) Dissipation versus frequency shift for sample replicate. The dashed and dotted arrows highlight the direction of increasing time/frequency shift and the difference in slope associated with each phase of fouling; (D) Sample frequency (D-1) and dissipation shifts (D-2) for fouling and cleaning processes (pre-rinse and caustic rinse only) for foulants formed at 0.1 mL/min. Curves represent the average of overtone-normalized frequency and dissipation shifts for the 5th, 7th, and 9th overtones (n = 5,7,9).

3.1.3 Bent-cable model of frequency shift during fouling

To quantify fouling and the effects of flow rate and protein concentration, a bent-cable model (Eq. 1)[32] was used to fit the frequency curve where the five model parameters carry physical significance in describing the fouling process (Figure 4). The application of this model does not consider the dissipation curve and assumes the frequency shift is linearly proportional to the areal mass density. Therefore, decreasing frequency shift is indicative of increasing areal mass density (mg/m^2) as described by the Sauerbrey model.

Figure 4 illustrates how the five model parameters of the bent-cable model quantify the rate of each fouling phase, the time point and frequency shift where the transition between phases occurs, and the rate of transition between phases. Here, the meaning of each parameter will be described in brief. First, α [s] describes the time of the 'breakpoint' or transition between Phase-1 and Phase-2. β_0 [Hz] quantifies the frequency shift this breakpoint, while γ [1, dimensionless] describes the curvature or rate transition at the breakpoint. Finally, the relationship between β_1 and β_2 define the slopes of Phase-1 ($m_1 = \beta_1 - \beta_2$, [Hz/s]) and Phase-2 ($m_2 = \beta_1 + \beta_2$, [Hz/s]).

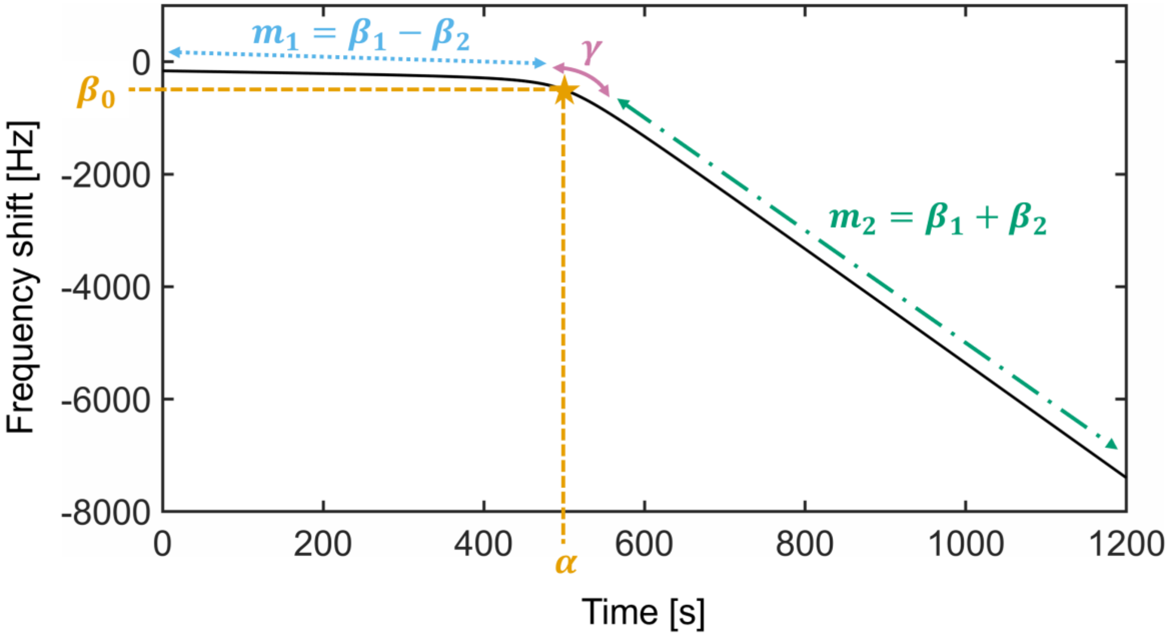

Figure 4. Visualization of bent-cable model and physical meaning of 5 model parameters: β_0 = -250 Hz, α = 500 s, γ = 100, β_1 = -5.2 Hz/s, and β_2 = -5 Hz.

3.1.4 Analysis of bent-cable model parameters

Average parameter values for the treatments can be found in Table 1 and goodness-of-fit measures (SSE, RMSE, and R^2) for the model fits are described in Table S4. The rate of Phase-1, m_1, is approximately doubled when the flow rate doubles for a given sample (17.5 or 35 g/L). In addition, β_0 follows this trend. The average values of α and γ are similar among all treatments. The rate of Phase-2, m_2, is much greater than the rate of Phase-1, m_1 (30–70X higher depending on the treatment), with a higher rate at 0.2 mL/min than 0.1 mL/min for a given sample (17.5 or 35 g/L). The nonlinearity of the initial fouling of 17.5 g/L samples, especially at 0.1 mL/min, was a source of greater variability in β_0 and m_1 because the bent-cable model cannot describe this nonlinearity (Figure S2, inset graph).

Table 1. Summary of fitted model parameters from bent-cable model[a]

Protein Concentration (g/L)	Flow Rate (mL/min)	β_0 [Hz]	α [s]	m_1 [Hz/s]	m_2 [Hz/s]	γ [1]
17.5	0.1	-183.9 ± 36.2	624.4 ± 52.0	-0.2576 ± 0.0773	-8.491 ± 0.4837	99.08 ± 6.21
17.5	0.2	-237.7 ± 8.4	511.6 ± 71.2	-0.3722 ± 0.0415	-10.94 ± 0.5867	87.72 ± 16.08
35	0.1	-138.9 ± 31.6	693.5 ± 30.1	-0.1661 ± 0.0263	-6.861 ± 0.6463	139.1 ± 17.98
35	0.2	-302.5 ± 21.3	618.1 ± 89.0	-0.4010 ± 0.0487	-8.763 ± 1.400	84.54 ± 13.27

[a] Model parameters are described as average ± SEM of N = 3 for 35 g/L and N = 4 for 17.5 g/L. Fitting was performed for the average frequency shift (n = 5,7,9)

An ANOVA was performed on each model parameter with the main effects of protein concentration and flow rate, as well as the interaction effect of between protein concentration and flow rate, which were all classified as discrete variables. The results showed a significant effect (p <0.05) of the main effect of flow rate on Slope 1 (p = 0.0105) and β_0 (p = 0.0048). But these model parameters (Slope 1 and β_0) were not significantly affected by the main effect of protein concentration. In comparison, there was a significant effect of flow rate (p = 0.0129) and protein concentration (p = 0.0283) on Slope 2. There was no significant effect of the treatments on the breakpoint, α, or γ.

When comparing differences between flow rates at a given protein concentration, m_1 and β_0 follow expectations for the effect of mass transfer with the values being approximately doubled when the flow rate is doubled, yet m_2 shows a more complex dependency on flow rate and protein concentration. To understand how these results describe the mechanism of fouling in QCM-D, thermal process design at QCM-D and industrial scales should be considered. An increase in flow rate on a pilot/commercial scale would result in an increase in hold-tube length to ensure an equivalent processing or residence time at a given hold temperature.[52] But there is no way of varying the length of the flow path in the HPHT QCM-D flow module, meaning doubling the flow rate also decreases the residence time by a factor of two at 135 °C.

Residence time is expected to affect the extent of reactions (i.e., protein denaturation, mineral precipitation) during thermal processing of milk;[53,54] therefore, in QCM-D, not only does flow rate change the rate of mass transfer, but it also effects the extent of chemical reactions. For example, 0.2 mL/min results in a higher rate of mass transfer than 0.1 mL/min, but reaction time or residence time is lower for 0.2 mL/min. Given the change in residence time and the negligible effect of physical forces within the QCM-D flow module due to laminar flow (Re <4), manipulation of flow rate at a QCM-D scale is expected to have a much greater effect on chemical reactions than at a larger scale. Therefore, the complex dependency in the rate of Slope 2 is likely due to the interactions between extent of reaction or residence time and mass transfer.

When comparing the fouling behavior at different protein concentrations, the 17.5 g/L samples show greater Phase-2 fouling rates than the 35 g/L samples at both flow rates. This is contradictory to previous fouling research where increasing protein content, specifically whey protein concentration, has been found to significantly increase the rate of fouling under HTST conditions.[55] In addition, increasing the protein content also increases the calcium content. Higher calcium contents in 35 g/L samples compared to the 17.5 g/L samples were also expected to increase rates of fouling, especially given the significant mineral contribution to the composition of UHT foulants.[56] A likely explanation for this unexpected trend is due to differences in contributions to the frequency shift for each sample beyond the adsorbed mass. The frequency shift describes both fouled components (i.e., proteins and minerals) as well as trapped water. A greater contribution of trapped water in foulants formed by the 17.5 g/L samples compared to the 35 g/L samples could ‘inflate’ the frequency shift.[40,42] Greater trapped water in the 17.5 g/L deposits may also be the source of exponential rise in dissipation with increasing frequency observed in the ΔD vs. ΔF curves (Figure 3C), compared to a relatively constant dissipation shift with increasing frequency for the 35 g/L deposits. This emphasizes the need to determine the contribution of coupled water before making comparisons between the 35 and 17.5 g/L samples. *In-situ* applications of optical techniques under continuous flow, such as ellipsometry (ELM), optical waveguide lightmode spectroscopy (OWLS), or surface plasmon resonance (SPR), are challenging under the current operational conditions (high temperatures and pressures), but application of these technologies to measure the dry mass thickness at numerous time-points within the fouling process can provide an estimate of the contributions of trapped water to a QCM-D response.[41,57]

3.2 *Multi-method analysis of irreversible fouling layers*

The drastic differences in cleaning behavior as a function of fouling formation flow rate (0.1 or 0.2 mL/min) motivated further investigation of the irreversible fouling layers. In this section, the samples resulting in the most fouling as measured by the frequency curve, 17.5 g/L at 0.1 and 0.2 mL/min, were selected for analysis. At a flow rate of 0.1 mL/min, fouling could be conducted for 20 mins, but for 0.2 mL/min over-dampening of the sensor was observed at 20 mins, so fouling runs were shortened to 18 mins to preserve frequency and dissipation data (N = 2).

3.2.1 Variable topography characterized by 3-D laser scanning microscopy (LSM)

To characterize differences in deposit appearance as a function of flow rate, 3-D LSM was used to take images of the deposit surface (Figure 5) along the centerline of the flow path (from inlet to outlet) (#4 in Figure 2).

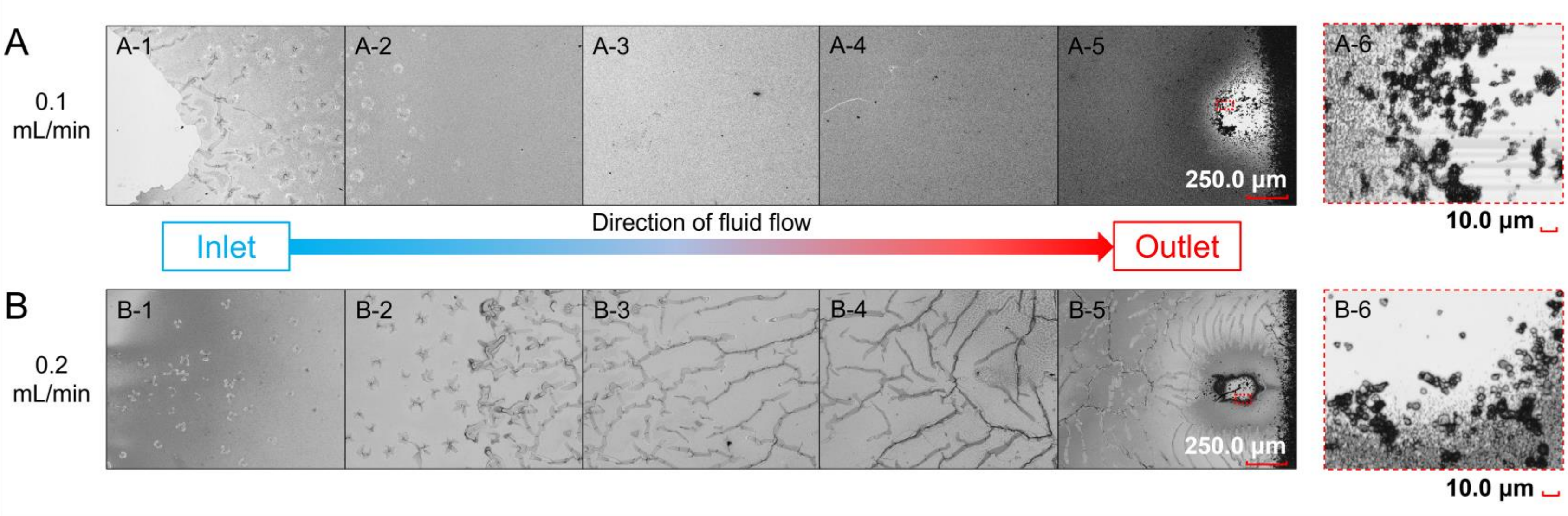

Figure 5. 3-D scanning laser microscopy of dried irreversible fouling layers. 10X images were collected after water rinse for fouling formed at (A) 0.1 mL/min and (B) 0.2 mL/min with 17.5 g/L MPC at 135 °C. Fouling layers were characterized in sequential progression from where fluid flows into the QCM-D chamber ('inlet' = A-1 and B-1) to where it exits ('outlet' = A-5 and B-5) at 5 approximately equidistant locations. Suspected hydroxyapatite grape-like clusters concentrated near outlet of sensor at 28x zoom for (A-6) 0.1 mL/min and (B-6) 0.2 mL/min. A-6 and B-6 images are increased magnification of images A-5 (outlet 0.1 mL/min) and B-5 (highlighted by red-dashed box).

The deposit formed at the higher flow rate (0.2 mL/min, Figure 5B) had numerous cracks, whereas the deposit formed at the lower flow rate (0.1 mL/min, Figure 5A) appeared grainy and close packed. This difference in topography supports the difference in cleaning behavior measured by HPHT QCM-D. Cracks in the deposit formed at 0.2 mL/min (Figure 5B) would be expected to increase the deposits' susceptibility to removal by NaOH as evidenced by the rapid swelling (Figure S8). This is in contrast to the close-packed deposits formed at 0.1 mL/min which were more resistant to removal by NaOH (Figure 5A).

Grape-like clusters of particles were concentrated near the outlet (Figure 5A-6 and B-6). These particles resemble those reported as hydroxyapatite (HAP),[58] which is a crystalline phase of calcium phosphate (CaP). The presence of these particles encouraged investigation of the fluid dynamics associated with the flow chamber.

3.2.2 Flow characteristics modeled by computational fluid dynamics (CFD)

To better understand the differences in microscopic topography determined by 3-D LSM, a CFD model of the HPHT QCM-D flow chamber was generated using COMSOL Multiphysics. The velocity distribution at each flow rate was visualized by velocity contours across the sensor surface at the center cut plane, as well as the local velocity and residence time distributions along the center line of flow (Figure 6).

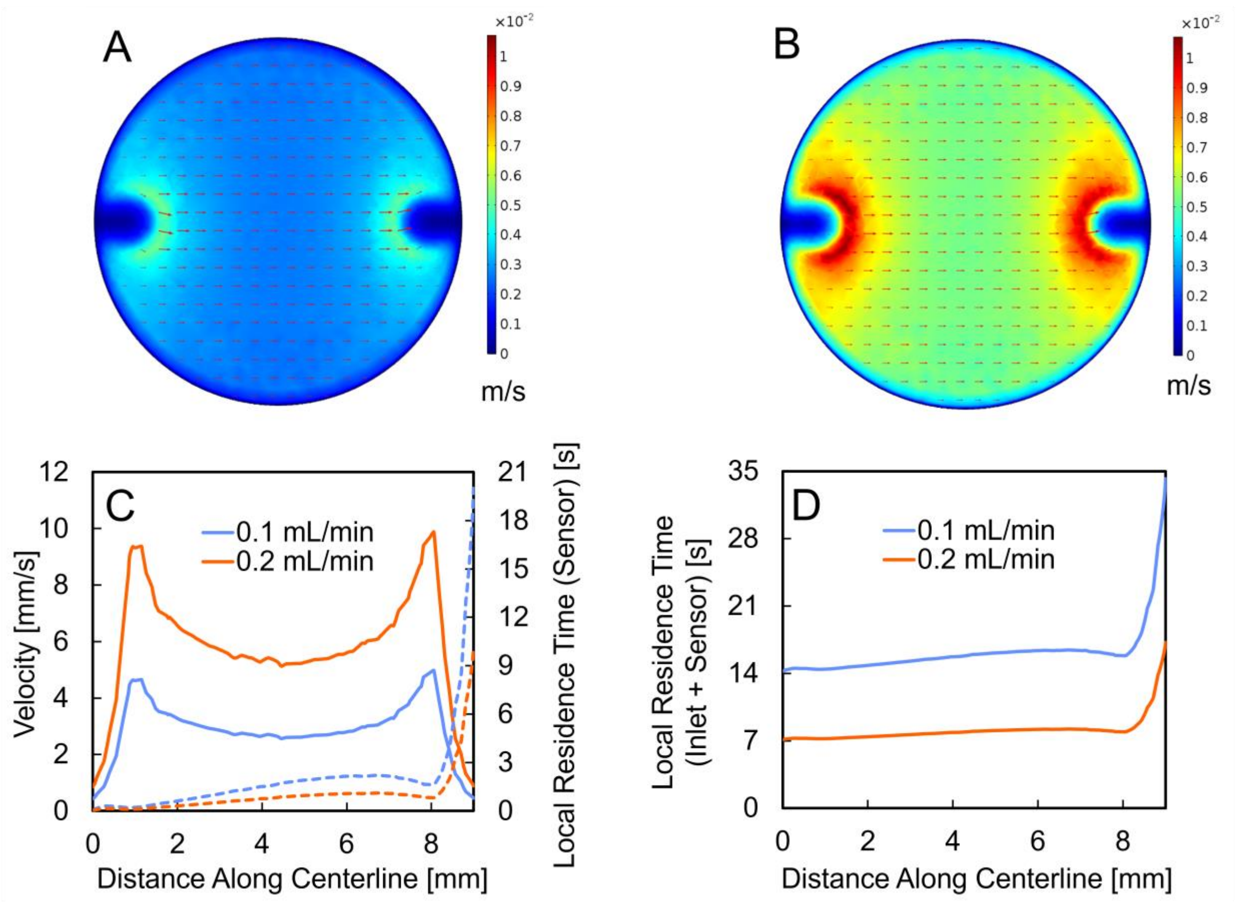

Figure 6. Computational fluid dynamics results. Velocity contours at the center plane for (A) 0.1 mL/min and (B) 0.2 mL/min. The color scale on the right describes the magnitude of the velocity from maximum in red (1.1E–2 m/s) to minimum in blue (0 m/s). The red arrows illustrate the directions of the local velocity vectors. These results were extracted from cut plane at ½ height of center of flow chamber (Figure S3). (C) Magnitude of local velocity (left axis, solid lines) and sensor residence time (right axis, dashed line) across the centerline of flow (#4 in Figure 2) from the center of the inlet (x = 0 mm) to the center of the outlet (x = 9 mm). This representation of local residence time does not consider the additive effect of inlet residence time in Eq. 2. (D) Local residence time with added effect of residence time spent in inlet tubing.

Figure 6A-B illustrate less variability in velocity near the center of the sensor where mass sensitivity is maximized.[59,60] The greatest variability in velocity occurs near the inlet and outlet where fluid expands and contracts, respectively. Maximum velocity is achieved just past the center of the inlet (~1 mm) and before the center of the outlet (peaks in velocity lines in Figure

6C), but the areas near the center of the inlet (0 to 0.5 mm distance along centerline) and just after the center of the outlet (8.5 to 9 mm distance along centerline) are characterized by a rapid decrease in velocity and flow is expected to be very stagnant in these locations.

The local residence time profiles along the centerline near the sensor surface without consideration of the residence time spent in the inlet (Figure 6C, dashed lines) are <2 s for both flow rates until approaching the center of the outlet (9 mm) where residence time rises exponentially due to the exponential decrease in velocity in this location. There is increased separation in local residence time when considering the residence time spent in the inlet tubing (#1 in Figure 2A). Here, the residence time spent in the inlet tubing has an additive effect of 14.2 s and 7.1 s for 0.1 and 0.2 mL/min, respectively. The lengthy inlet tubing in this QCM-D device ensures isothermal conditions between the sample and sensor surface in the inlet chamber, but it also has a significant impact on total residence time (Figure 6C vs. Figure 6D). The pressure drop along the centerline of flow for 0.1 and 0.2 mL/min was 2.9 and 5.8 Pa, respectively (Figure S13). In addition, derived values (i.e., maximum/average velocities, Reynolds numbers, etc.) are described in Table S5.

The deposition of HAP near the outlet (Figure 5A-6 and B-6) can be explained by fluid dynamics and residence time. Just past the front of the outlet, the velocity drops drastically (Figure 6C). This low velocity or stagnation of flow would be expected to promote the deposition of large particles such as HAP. In addition, the local residence is maximum just past the front of the outlet (Figure 6C-D) because its location is farthest from the inlet and velocity is low. The low velocity and limited in-line mixing in QCM-D equates to a batch-type reactor. For batch crystallizers, long residence times increase the median particle size[61] which may explain the large HAP particles observed near the outlet.

The results of this CFD model and the inverse relationship between residence time and mass transfer may explain differences in topography observed between the two fouling flow rates. Fouling can be described as a combination of mass transfer and chemical reaction steps including (1) reactions within the bulk fluid (i.e., protein denaturation and aggregation, and mineral precipitation), (2) mass transfer of these reacted components to the surface, (3) surface reactions which lead to the incorporation of reacted components into the fouling matrix, and (4) possible transfer of reacted components back to the bulk.[62] Extent of chemical reactions within Steps 1 and 3 of this process are expected to be maximized for the 0.1 mL/min, whereas rates of mass transfer in Steps 2 and 4 are expected to be maximized for the 0.2 mL/min sample. Step 3 may be the most important in explaining differences in deposit topography. Increased surface reaction time for the foulant formed at 0.1 mL/min would be expected to lead to enhanced incorporation of reacted species and thus a more close-packed structure, when compared to the highly cracked structure formed at 0.2 mL/min.

3.2.3 Chemical composition revealed by Raman Spectroscopy

Raman spectroscopy was used for qualitative identification of major fouling components. Raman spectra were collected at numerous locations across the centerline of the sensor. A comparison of representative spectra from each flow rate at two different locations is depicted in Figure 7. There are negligible differences in the frequencies of the Raman bands when comparing spectra from the different flow rates collected at similar locations, indicating that the signals arise from similar, if not identical, species present on the sensor surfaces at different flow rates. Therefore, despite the differences in structure observed by microscopy (Figure 5), the foulants formed at different flow rates are similar in composition. Additional Raman spectra were collected near the inlet and in numerous center locations (results not plotted in Figure 7, see SI, Figures S14-S17, for Raman spectra of all replicates), but the peaks align with those found for the ‘center’ sample. Broadly, the peaks define a heterogenous fouling layer comprised primarily of calcium phosphate (CaP) and protein.

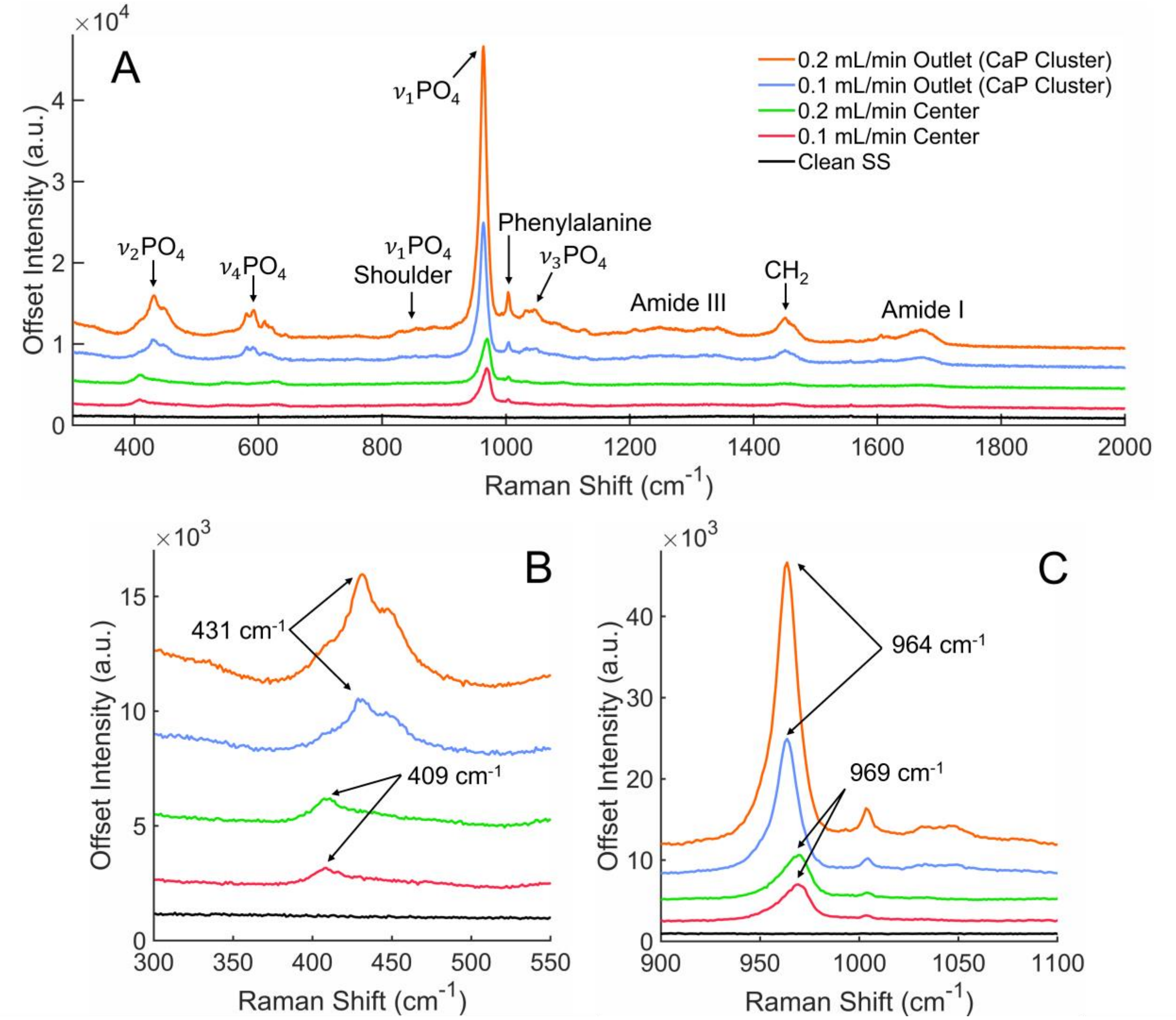

Figure 7. Sample Raman spectra for UHT milk deposits formed by 17.5 g/L MPC at 135 °C and at different flow rates (0.1 and 0.2 mL/min). Raman spectra were at different locations on the stainless steel QCM-D sensor. 'Center' spectra were collected at the approximate radial center of the sensor. 'CaP clusters' spectra were collected at the visible calcium phosphate clusters concentrated near the outlet of the flow chamber. (A) Wide scan spectra highlighting noteworthy Raman peaks characteristic of calcium phosphate and protein. (B) Closer look at ν_2PO_4 symmetric stretch showing shift in peak location from 409 cm^{-1} for 'Center' samples to 431 cm^{-1} for 'CaP Clusters' samples. (C) Closer look at ν_1PO_4 asymmetric stretch showing shift in peak location from 969 cm^{-1} for 'Center' samples to 964 cm^{-1} for 'CaP cluster' samples.

The symmetric and asymmetric bending and stretching modes of PO_4^{3-} provide CaP and its crystalline phases with a distinct chemical fingerprint,[63–65] allowing different phases to be identified at different locations across the sensor surface. Figure 7B-C illustrates distinct shifts in peak locations for some vibrational modes of PO_4^{3-} and Table 2 specifies peak locations for all four vibrational modes. The CaP crystalline phase of prominent grape-like clusters concentrated at the outlet (Figure 5) was identified to be closest to hydroxyapatite (HAP). But shifts in peak location in spectra collected near the inlet, at numerous locations in the center, and just before the outlet of the sensor, indicate the presence of a different crystalline phase, β-tricalcium phosphate (β-$Ca_3(PO_4)_2$, β-TCP).[66] These findings are consistent with composition analysis (via X-ray diffraction) of UHT foulants (137 ° C) at an industrial scale[56,67] where the predominant fouling component was CaP, specifically in the crystalline form of β-TCP. From a thermodynamic standpoint, the most favorable phase of calcium phosphate is HAP;[68] therefore, there is a need for more research to understand why β-TCP is the predominant CaP phase formed in UHT milk fouling deposits.

Table 2. Raman shift associated with PO_4^{-3} vibrational modes for fouling layers (17.5 g/L at 0.1 and 0.2 mL/min) and known crystalline calcium phosphate phases

PO_4^{-3-} vibrational mode	Range of approx. Raman Shift (cm^{-1})	Identifiable Raman Peaks (cm^{-1})			
		Inlet/Center[a]	Outlet[a]	HAP[69]	β-TCP[69]
$\nu_1 PO_4^{-3-}$	930-990	969	964	962	946, 949, 961, 970
$\nu_2 PO_4^{-3-}$	400-490	409	431	430, 447, 452	405, 439, 460, 475, 483
$\nu_3 PO_4^{-3-}$	1020-1095	1033, 1041 1086, 1096	1033, 1047	1029, 1033, 1043, 1048, 1054, 1077	1005, 1016, 1031, 1038, 1046, 1059, 1074, 1091
$\nu_4 PO_4^{-3-}$	550-630	551, 624, 631	581, 591, 609	579, 588, 591, 594, 607, 615	547, 555, 578, 588, 599, 611, 624, 631

[a]includes both 0.1 and 0.2 mL/min samples

In addition to calcium phosphate, protein signals were detected in all samples with peaks from phenylalanine (1003–1005 cm^{-1}) and bands in the amide I (1640–1680 cm^{-1}) and amide III (1200–1300 cm^{-1}) regions, which originate from the polypeptide backbone. In addition, peaks signifying a CH_2 (1420–1480 cm^{-1}) deformation were identified.[64,70,71] The exact amount of protein and mineral cannot be quantified without a proper standard, which may be explored in future studies. The mixture of protein and calcium phosphate identified in these deposits is consistent with previous research where the chemical composition of a UHT foulant was identified a mixture of calcium phosphate (71%) and protein (11%).[56]

The composition of the 17.5 g/L deposits also helps explain the cleaning behavior of these deposits measured by HPHT QCM-D. The swelling exhibited by foulants formed at both flow rates is indicative of the presence of protein which is confirmed by Raman spectroscopy. In addition, for fouling formed at 0.1 mL/min, where cleaning data was retained after the addition of 0.1 M NaOH, the high concentration of CaP explains why this foulant is not easily cleaned by 0.1 M NaOH which is unable to solubilize inorganic material. Without a proper standard to quantitatively compare the protein concentration in both foulants, differences in swelling behavior between the foulant formed at 0.1 mL/min and 0.2 mL/min cannot definitively be attributed to a higher protein concentration in the 0.2 mL/min foulant compared to the 0.1 mL/min foulant. But an argument based on structural differences could be used to explain differences in cleaning behavior. Due to increased residence time, the deposits formed at 0.1 mL/min are more compact making it more difficult for 0.1 M NaOH to diffuse and solubilize protein. Whereas with the higher flow rate, 0.2 mL/min, the brittle and cracked structure allows 0.1 M NaOH to diffuse easier through the foulant matrix.

Many fouling studies attempt to determine which deposits first, protein or mineral. Answering this question is challenging for the present study because the form of Raman spectroscopy used in the present study provides a composite signal from all molecules within the ~1 µm laser spot and lacks the spatial resolution to determine fouling gradients that may form.

3.2.4 Structural differences amplified by atomic force microscopy (AFM)

AFM was used to characterize the topography and dry thickness of the irreversible fouling layers. The structural heterogeneity across the centerline of flow observed by microscopy is further illuminated by AFM with increased sensitivity and quantitative measures of topography (i.e., surface roughness). Figure 8 shows representative images for changes in topography at three different locations ranging from the center of the inlet to the center of the outlet for 17.5 g/L at each flow rate. Taking samples from different locations along the centerline of the flow path evaluates the effects of residence time because deposits formed near the inlet are from milk receiving the least amount of heat treatment compared to deposits at the outlet where the residence time is the greatest. The roughness (Ra) of the clean control was 0.86 ± 0.01 nm (average ± SEM of 3 subreplicates).

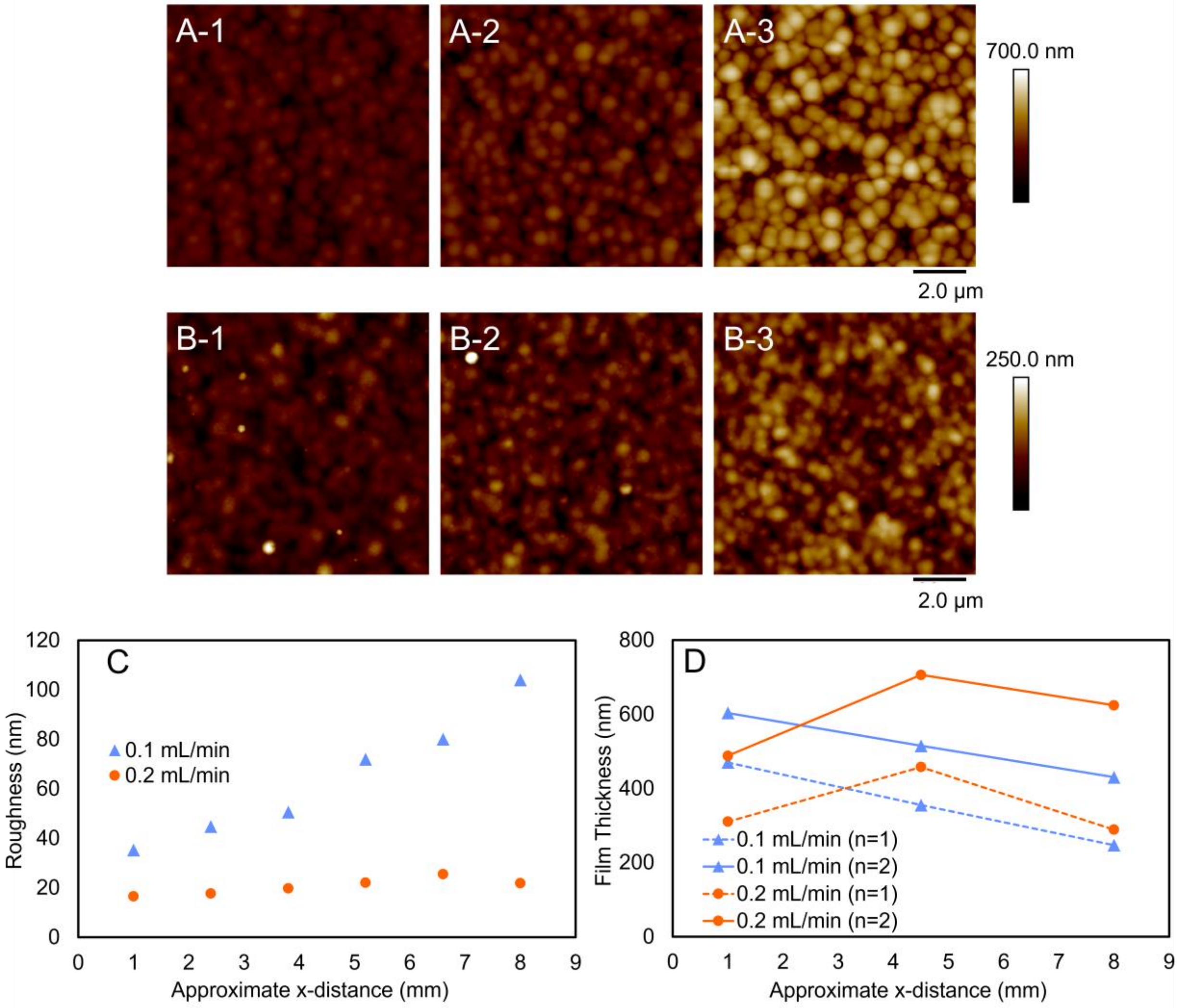

Figure 8. Atomic force microscopy (AFM) characterization of roughness and thickness for irreversible fouling layers (17.5 g/L MPC and 135°C) formed different flow rates (0.1 and 0.2 mL/min). AFM height sensor for (A) 0.1 mL/min with a maximum scale of 700 nm and (B) 0.2 mL/min with a maximum scale of 250 nm at three approximately equidistant locations corresponding to x = 1, 3.8, 8 mm in (C). (C) Change in average roughness (R_a) at six approximately equidistant locations for a representative replicate, progressing from the center of the inlet (x = 0 mm) to center of the outlet (x = 9mm). Additional replicate is presented in SI (Figure S19). The R_a of the clean control was 0.86 nm. (D) Change in fouling layer thickness at three approximately equidistant locations for all replicates, progressing from the center of the inlet (x = 0 mm) to center of the outlet (x = 9mm)

Figure 8, especially Figure 8A–3, defines a matrix of discrete particles. Based on Raman spectroscopy data, these particles are presumably crystals of β-TCP. Figure 8A–3 also shows the greatest definition and size of CaP particles at the lowest flow rate and longest residence time.[61] This suggests residence time is a critical parameter for the development and maturation of a UHT foulant.

Furthermore, there is a drastic difference in roughness scale when comparing flow rates; this is further illustrated by the average roughness values at six locations ranging from the center of the inlet to the center of the outlet for the different flow rates (Figure 8C). Average roughness is a measure of apparent surface properties which quantifies the arithmetic mean of height deviations above and below the mean height.[72] Therefore, average roughness is not a measure of total fouling layer thickness which is the difference in height between the bare stainless steel and average surface height of the foulant.

Using a 'scratching' technique, dry fouling layer thickness was also measured using AFM (Figure 8D). The decreasing foulant thickness behavior for foulants formed at 0.1 mL/min can be explained by DLVO theory, which supports that the energy or steric barrier for interaction between a particle and the surface increases with increasing particle size or coverage.[73,74] If calcium phosphate particles first precipitate in the bulk fluid and are transported to the surface, it is easier for smaller particles, which are those formed at the smallest residence time near the inlet (x = 1 mm, Figure 8D), to adhere to the surface than larger particles formed due to increased residence time near the outlet (x = 8 mm, Figure 8D). The foulant thickness trend across the centerline for 0.2 mL/min presents a more complex relationship. The results may represent competition between fluid dynamics and DLVO theory. Constant, low velocity flow, concentrated at the center of the crystal (Figure 6) results in low wall shear stresses which would be expected to produce the greatest foulant thickness. This is compared to locations near the inlet and outlet where high velocity and thus higher wall shear stress, as well as large particles due to points of flow stagnation, would result in decreased foulant thickness. The roughness and foulant thickness results in Figure 8C-D are plotted as a function of sampling location, but these results can be plotted against the approximate local residence time (Figure S18). When normalized to approximate residence time, the trend in foulant thickness aligns between treatments with decreasing thickness after ~5 s, but treatments still show differences when comparing trends in roughness.

AFM scans were also performed on the HAP clusters near the outlet (Figure 9A-C). The large diameter of these particles was measured using the AFM analysis software, enabling comparisons of particle size and surface roughness. There was a trend of increasing deposit roughness with increasing average particle size (Figure 9D). These results align with a previous work which presents a fouling mechanism where the presence of discrete calcium carbonate particles enhances the overall surface roughness of the sample resulting in preferential cracks and crevices for further fouling.[34] Observations of increasing β-TCP particle size (Figure 8A-B) and increasing roughness (Figure 8C) across the centerline of flow, in addition to the correlation between particle size and roughness presented in Figure 9, support increasing CaP particle size with increased residence time.

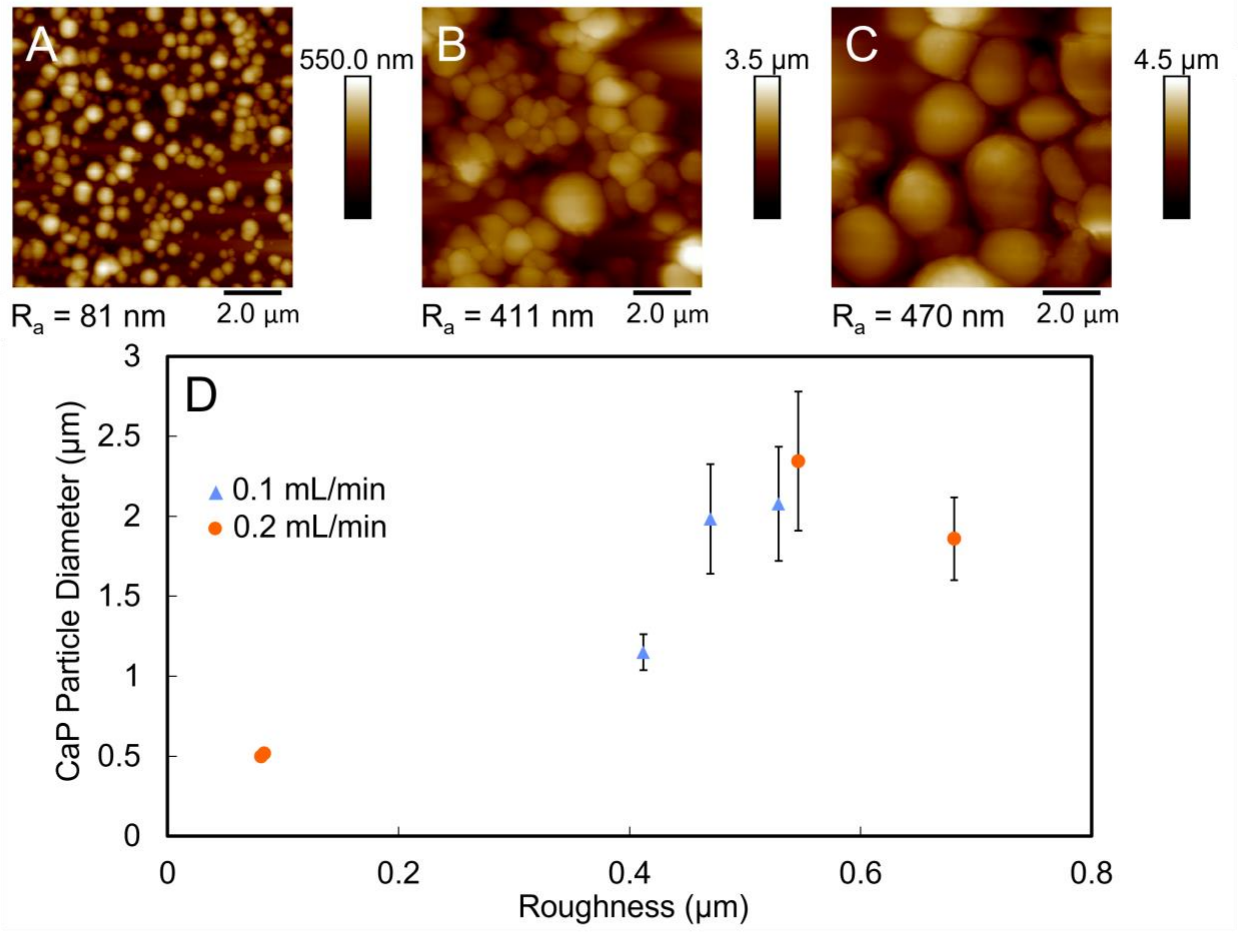

Figure 9. Change in average surface roughness as a function of calcium phosphate particle size. (A)-(C) show sample images used for particle size estimation from calcium phosphate clusters concentrated on stainless-steel surface at outlet of flow chamber (A-6 and B-6 in Figure 5). The height scale (to the right of image) and average roughness value (R_a, below image) increase from (A) to (C). (D) shows trend between calcium phosphate (CaP) particle diameter and average surface roughness. Error bars represent 95% confidence interval for average particle diameter.

4. Conclusions

This investigation of foulants formed during a ultra-high temperature (UHT) process for a milk-based model fluid at different protein concentrations and flow rates provided several conclusions which, without the use of nano- and micro-scale techniques, may have been otherwise undetectable if studied at larger scales.

Notably, two-phases of fouling were discriminated and modelled by a five-parameter bent-cable model. The rate of fouling during Phase-1 was statistically dependent on flow rate, while the rate of fouling during Phase-2 was statistically dependent on flow rate and protein concentration. These observations could not distinguish whether mass transfer and/or chemical reactions were the driving force of fouling because flow rate, which is traditionally associated with mass transfer on larger scales, is coupled to reaction or residence time in the QCM-D device. Changes in the flow rate in QCM-D research, specifically during high-temperature applications, have implications beyond changes in mass transfer because flow rate significantly affects residence time and the extent of chemical reactions.

Physical and chemical characteristics of the irreversible fouling layers formed at a protein concentration of 17.5 g/L were significantly affected by flow rate, and thus the residence time, during fouling. The predominate components of the foulant formed at both flow rates were identified as β-tricalcium phosphate (β-TCP) and protein. In addition, hydroxyapatite (HAP) particles were distinguished near the outlet of the flow device. This composition was consistent with the composition of UHT foulants identified in previous studies at larger scales which supports the use of HPHT QCM-D to study industrially relevant foulants.

An open and cracked topography was observed for deposits formed at the higher flow rate where residence time is minimized, as compared to a close-packed topography for deposits formed at the lower flow rate where residence time is maximized. Differences in topography were linked to cleaning behavior observed with QCM-D. The cracked and brittle foulant from the high flow rate treatment was more susceptible to swelling during cleaning with 0.1M NaOH than the foulant formed at the low flow rate.

The combination of real-time fouling and cleaning monitoring techniques, as well as fouling characterization methods at nano- and micro-scales, suggest that processing conditions, specifically flow rate and residence time, not only influence the rate of fouling, but also the structure and topography of the foulant. Overall, these conclusions provide insight into the first interactions between a complex food matrix and a stainless-steel surface at ultra-high temperatures. The conditions of this first interaction are crucial to the structure and growth of the deposit, which ultimately has implications for the removal of this deposit during CIP operations. This connection between fouling and cleaning behavior challenges current cleaning practices, by converting 'one-size-fits-all' cleaning protocols into targeted cleaning protocols that 'meet the needs' of the foulant with minimal water, chemical, and energy usage.

ASSOCIATED CONTENT

Supporting_Information_for_Publication.docx: compositional details of milk protein concentrate (MPC), physical pictures of system, non-linear least squares fitting algorithm, location of COMSOL cut-planes and cut-lines, standard deviation between harmonics of frequency and dissipation curves, sample frequency and dissipation shift at multiple overtones, sample acoustic ratio (AR) and table of average/max AR at different time points, goodness-of-fit for bent-cable model, frequency and dissipation curves during fouling and cleaning for all replicates, additional COMSOL results (pressure distribution and summary table), Raman spectra from all locations, comparison of roughness and thickness to local residence time, additional replicate of surface roughness data.

AUTHOR CONTRIBUTIONS

H.H., N.E., and D.H. designed the research. H.H. led writing of the manuscript and performed all experiments with the exception of assistance from T.P. in collection of the Raman spectroscopy results. T.P. and Z.S. assisted in the presentation and interpretation of the Raman spectroscopy results. All authors reviewed and revised the manuscript.

FUNDING SOURCES

The HPHT QCM-D equipment was supported partially by the Center for Advanced Processing and Packaging Studies CAPPS, an NSF IUCRC Founded Center. The Dale A. Seiberling endowment of the Food Engineering Laboratory at the Ohio State University (OSU) supported supplies and equipment user-fees. National Science Foundation Award CHE-2107791 to Z.S. supported the Raman spectroscopy experiments.

ACKNOWLEDGMENTS

The authors would like to acknowledge:

- Fredrik Pettersson and his colleagues at Biolin Scientific for providing dimensions associated with the high-pressure flow module using in computational fluid dynamics modelling.
- Archana Jaiswal of Nanoscience Instruments for her assistance in training and method development in use of the HPHT QCM-D.
- Dr. Rafael Jimenez-Flores (Department of Food Science and Technology, OSU) for the use of his QCM-D electronics unit and accessories, as well as his 3-D scanning laser microscope.
- Milk Specialties (Eden Prairie, MN, USA) for the donation of milk protein concentrate.

ABBREVIATIONS

HPHT QCM-D, High-pressure high temperature quartz crystal microbalance with dissipation; UHT, ultra-high temperature; HTST, high-temperature short-time; CIP, clean-in-place; SS, stainless steel; AFM, atomic force microscope; CFD, computational fluid dynamics; CaP, calcium phosphate; HAP, hydroxyapatite; β-TCP, β-tricalcium phosphate; MPC, milk protein concentrate; LSM, laser scanning microscopy.

REFERENCES

(1) Khaldi, M.; Croguennec, T.; André, C.; Ronse, G.; Jimenez, M.; Bellayer, S.; Blanpain-Avet, P.; Bouvier, L.; Six, T.; Bornaz, S.; Jeantet, R.; Delaplace, G. Effect of the Calcium/Protein Molar Ratio on β-Lactoglobulin Denaturation Kinetics and Fouling Phenomena. *Int. Dairy J.* **2018**, 78, 1–10. DOI: 10.1016/j.idairyj.2017.10.002.

(2) Zhang, B. Y.; Lu, J.; Huang, J. Y. Effect of Sugar on the Fouling Behavior of Whey Protein. *Food Bioprod. Process*. **2019**, 113, 2–9. DOI: 10.1016/j.fbp.2018.10.002.

(3) Bouvier, L.; Fargnier, I.; Lalot, S.; Delaplace, G. Effect of Swirl Flow on Whey Protein Fouling and Cleaning in a Straight Duct. *J. Food Eng*. **2019**, 242, 115–123. DOI: 10.1016/j.jfoodeng.2018.08.024.

(4) Gillham, C. R.; Fryer, P. J.; Hasting, A. P. M.; Wilson, D. I. Enhanced Cleaning of Whey Protein Soils Using Pulsed Flows. *J. Food Eng*. **2000**, 46 (3), 199–209. DOI: 10.1016/S0260-8774(00)00083-2.

(5) Ávila-Sierra, A.; Zhang, Z. J.; Fryer, P. J. Effect of Surface Roughness and Temperature on Stainless Steel - Whey Protein Interfacial Interactions under Pasteurisation Conditions. *J. Food Eng*. **2021**, 301, 110542. DOI: 10.1016/j.jfoodeng.2021.110542.

(6) Zouaghi, S.; Six, T.; Nuns, N.; Simon, P.; Bellayer, S.; Moradi, S.; Hatzikiriakos, S. G.; André, C.; Delaplace, G.; Jimenez, M. Influence of Stainless Steel Surface Properties on Whey Protein Fouling under Industrial Processing Conditions. *J. Food Eng*. **2018**, 228, 38–49. DOI: 10.1016/j.jfoodeng.2018.02.009.

(7) Tsai, J. H.; Huang, J. Y.; Wilson, D. I. Life Cycle Assessment of Cleaning-in-Place Operations in Egg Yolk Powder Production. *J. Clean. Prod*. **2021**, 278, 123936. DOI: 10.1016/j.jclepro.2020.123936.

(8) Tiwari, S.; Behera, C. R.; Srinivasan, B. Simulation and Experimental Studies to Enhance Water Reuse and Reclamation in India's Largest Dairy Industry. *J. Environ. Chem. Eng*. **2016**, 4 (1), 605–616. DOI: 10.1016/j.jece.2015.12.001.

(9) Wilson, D. I. Fouling during Food Processing – Progress in Tackling This Inconvenient Truth. *Curr. Opin. Food Sci*. **2018**, 23, 105–112. DOI: 10.1016/j.cofs.2018.10.002.

(10) Goode, K. R.; Bowen, J.; Akhtar, N.; Robbins, P. T.; Fryer, P. J. The Effect of Temperature on Adhesion Forces between Surfaces and Model Foods Containing Whey Protein and Sugar. *J. Food Eng*. **2013**, 118 (4), 371–379. DOI: 10.1016/j.jfoodeng.2013.03.016.

(11) Liu, W.; Fryer, P. J.; Zhang, Z.; Zhao, Q.; Liu, Y. Identification of Cohesive and Adhesive Effects in the Cleaning of Food Fouling Deposits. *Innov. Food Sci. Emerg. Technol*. **2006**, 7 (4), 263–269. DOI: 10.1016/j.ifset.2006.02.006.

(12) Fryer, P. J.; Asteriadou, K. A Prototype Cleaning Map: A Classification of Industrial Cleaning Processes. *Trends Food Sci. Technol*. **2009**, 20 (6–7), 255–262. DOI: 10.1016/j.tifs.2009.03.005.

(13) Goode, K. R.; Asteriadou, K.; Robbins, P. T.; Fryer, P. J. Fouling and Cleaning Studies in the Food and Beverage Industry Classified by Cleaning Type. *Compr. Rev. Food Sci. Food Saf*. **2013**, 12 (2), 121–143. DOI: 10.1111/1541-4337.12000.

(14) Herrera-Márquez, O.; Serrano-Haro, M.; Vicaria, J. M.; Jurado, E.; Fraatz-Leál, A. R.; Zhang, Z. J.; Fryer, P. J.; Avila-Sierra, A. Cleaning Maps: A Multi Length-Scale Strategy to Approach the Cleaning of Complex Food Deposits. *J. Clean. Prod*. **2020**, 261, 121254. DOI: 10.1016/j.jclepro.2020.121254.

(15) Reviakine, I.; Johannsmann, D.; Richter, R. P. Hearing What You Cannot See and Visualizing What You Hear: Interpreting Quartz Crystal Microbalance Data from Solvated Interfaces. *Anal. Chem*. **2011**, 83 (23), 8838–8848. DOI: 10.1021/ac201778h.

(16) Johannsmann, D. *The Quartz Crystal Microbalance in Soft Matter Research: Fundamentals and Modeling*; Springer, **2014**. DOI: 10.1007/978-3-319-07836-6.

(17) Johannsmann, D. Derivation of the Shear Compliance of Thin Films on Quartz Resonators from Comparison of the Frequency Shifts on Different Harmonics: A Perturbation Analysis. *J. Appl. Phys*. **2001**, 89 (11), 6356–6364. DOI: 10.1063/1.1358317.

(18) Huellemeier, H. A.; Eren, N. M.; Ortega-Anaya, J.; Jimenez-Flores, R.; Heldman, D. R. Application of Quartz Crystal Microbalance with Dissipation (QCM-D) to Study Low-Temperature Adsorption and Fouling of Milk Fractions on Stainless Steel. *Chem. Eng. Sci*. **2022**, 247, 117004. DOI: 10.1016/j.ces.2021.117004.

(19) Yang, W.; Li, D.; Chen, X. D.; Mercadé-Prieto, R. Effect of Calcium on the Fouling of Whey Protein Isolate on Stainless Steel Using QCM-D. *Chem. Eng. Sci*. **2018**, 177, 501–508. DOI: 10.1016/j.ces.2017.12.004.

(20) Avila-Sierra, A.; Huellemeier, H. A.; Zhang, Z. J.; Heldman, D. R.; Fryer, P. J. Molecular Understanding of Fouling Induction and Removal: Effect of the Interface Temperature on Milk Deposits. *ACS Appl. Mater. Interfaces* **2021**, 13 (30), 35506–35517. DOI: 10.1021/acsami.1c09553.

(21) Gotham, S. M.; Fryer, P. J.; Pritchard, A. M. Β-lactoglobulin Denaturation and Aggregation Reactions and Fouling Deposit Formation: A DSC Study. *Int. J. Food Sci. Technol*. **1992**, 27 (3), 313–327. DOI: 10.1111/j.1365-2621.1992.tb02033.x.

(22) Blanpain-Avet, P.; André, C.; Khaldi, M.; Bouvier, L.; Petit, J.; Six, T.; Jeantet, R.; Croguennec, T.; Delaplace, G. Predicting the Distribution of Whey Protein Fouling in a Plate Heat Exchanger Using the Kinetic Parameters of the Thermal Denaturation

Reaction of β-Lactoglobulin and the Bulk Temperature Profiles. *J. Dairy Sci*. **2016**, 99 (12), 9611–9630. DOI: 10.3168/jds.2016-10957.

(23) De Jong, P.; Bouman, S.; Van Der Linden, H. J. L. J. Fouling of Heat Treatment Equipment in Relation to the Denaturation of β-Lactoglobulin. *J. Soc. Dairy Technol.* **1992**, 45 (1), 3–8. DOI: 10.1111/j.1471-0307.1992.tb01715.x.

(24) Lalande, M.; Tissier, J. -P. Fouling of Heat Transfer Surfaces Related to β-Lactoglobulin Denaturation During Heat Processing of Milk. *Biotechnol. Prog*. **1985**, 1 (2), 131–139. DOI: 10.1002/btpr.5420010210.

(25) Sauer, A.; Moraru, C. I. Heat Stability of Micellar Casein Concentrates as Affected by Temperature and PH. *J. Dairy Sci*. **2012**, 95 (11), 6339–6350. DOI: 10.3168/jds.2012-5706.

(26) Campen, S.; Moorhouse, S. J.; Wong, J. S. S. Mechanism of an Asphaltene Inhibitor in Different Depositing Environments: Influence of Colloid Stability. *J. Pet. Sci. Eng*. **2020**, 184,106502. DOI: 10.1016/j.petrol.2019.106502.

(27) Tavakkoli, M.; Panuganti, S. R.; Taghikhani, V.; Pishvaie, M. R.; Chapman, W. G. Asphaltene Deposition in Different Depositing Environments: Part 1. Model Oil. *Energy and Fuels* **2014**, 28 (6), 1617–1628. DOI: 10.1021/ef401857t.

(28) Tavakkoli, M.; Panuganti, S. R.; Taghikhani, V.; Pishvaie, M. R.; Chapman, W. G. Asphaltene Deposition in Different Depositing Environments: Part 2. Real Oil. *Energy and Fuels* **2014**, 28 (6), 3594–3603. DOI: 10.1021/ef401868d.

(29) Joonaki, E.; Buckman, J.; Burgass, R.; Tohidi, B. Exploration of the Difference in Molecular Structure of n -C7 and CO2 Induced Asphaltenes. *Ind. Eng. Chem. Res*. **2018**, 57 (26), 8810–8818. DOI: 10.1021/acs.iecr.8b01634.

(30) Joonaki, E.; Burgass, R.; Hassanpouryouzband, A.; Tohidi, B. Comparison of Experimental Techniques for Evaluation of Chemistries against Asphaltene Aggregation and Deposition: New Application of High-Pressure and High-Temperature Quartz Crystal Microbalance. *Energy and Fuels* **2018**, 32 (3), 2712–2721. DOI: 10.1021/acs.energyfuels.7b02773.

(31) Kanazawa, K. K.; Gordon, J. G. Frequency of a Quartz Microbalance in Contact with Liquid. *Anal. Chem*. **1985**, 57, 1770–1771. DOI: 10.1021/ac00285a062.

(32) Toms, J. D.; Lesperance, M. L. Piecewise Regression: A Tool for Identifying Ecological *Thresholds. Ecology* **2003**, 84 (8), 2034–2041. DOI: 10.1890/02-0472.

(33) Otzen, D. E.; Oliveberg, M.; Höök, F. Adsorption of a Small Protein to a Methyl-Terminated Hydrophobic Surfaces: Effect of Protein-Folding Thermodynamics and Kinetics. *Colloids Surfaces B Biointerfaces* **2003**, 29 (1), 67–73. DOI: 10.1016/S0927-7765(02)00186-8.

(34) Jimenez, M.; Delaplace, G.; Nuns, N.; Bellayer, S.; Deresmes, D.; Ronse, G.; Alogaili, G.; Collinet-Fressancourt, M.; Traisnel, M. Toward the Understanding of the Interfacial Dairy Fouling Deposition and Growth Mechanisms at a Stainless Steel Surface: A Multiscale Approach. *J. Colloid Interface Sci*. **2013**, 404, 192–200. DOI: 10.1016/j.jcis.2013.04.021.

(35) Changani, S. D.; Belmar-Beiny, M. T.; Fryer, P. J. Engineering and Chemical Factors Associated with Fouling and Cleaning in Milk Processing. *Exp. Therm. Fluid Sci*. **1997**, 14 (4), 392–406. DOI: 10.1016/S0894-1777(96)00141-0.

(36) Singh, J.; Prakash, S.; Bhandari, B.; Bansal, N. Ultra High Temperature (UHT) Stability of Casein-Whey Protein Mixtures at High Protein Content: Heat Induced Protein Interactions. *Food Res. Int*. **2019**, 116, 103–113. DOI: 10.1016/j.foodres.2018.12.049.

(37) Foster, C. L.; Green, M. L. A Model Heat Exchange Apparatus for the Investigation of Fouling of Stainless Steel Surfaces by Milk II. Deposition of Fouling Material at 140 °C, Its Adhesion and Depth Profiling. *J. Dairy Res*. **1990**, 57 (3), 339–348. DOI: 10.1017/S0022029900026996.

(38) Sauerbrey, G. Verwendung von Schwingquarzen Zur Wägung Dünner Schichten Und Zur Mikrowägung. *Zeitschrift für Phys*. **1959**, 155 (2), 206–222. DOI: 10.1007/BF01337937.

(39) Carton, I.; Brisson, A. R.; Richter, R. P. Label-Free Detection of Clustering of Membrane-Bound Proteins. *Anal. Chem*. **2010**, 82 (22), 9275–9281. DOI: 10.1021/ac102495q.

(40) Höök, F.; Rodahl, M.; Brzezinski, P.; Kasemo, B. Energy Dissipation Kinetics for Protein and Antibody-Antigen Adsorption under Shear Oscillation on a Quartz Crystal Microbalance. *Langmuir* **1998**, 14 (4), 729–734. DOI: 10.1021/la970815u.

(41) Höök, F.; Vörös, J.; Rodahl, M.; Kurrat, R.; Böni, P.; Ramsden, J. J.; Textor, M.; Spencer, N. D.; Tengvall, P.; Gold, J.; Kasemo, B. A Comparative Study of Protein Adsorption on Titanium Oxide Surfaces Using in Situ Ellipsometry, Optical Waveguide Lightmode Spectroscopy, and Quartz Crystal Microbalance/Dissipation. *Colloids Surfaces B Biointerfaces* **2002**, 24 (2), 155–170. DOI: 10.1016/S0927-7765(01)00236-3.

(42) Höök, F.; Kasemo, B.; Nylander, T.; Fant, C.; Sott, K.; Elwing, H. Variations in Coupled Water, Viscoelastic Properties, and Film Thickness of a Mefp-1 Protein Film during Adsorption and Cross-Linking: A Quartz Crystal Microbalance with Dissipation Monitoring, Ellipsometry, and Surface Plasmon Resonance Study. *Anal. Chem*. **2001**, 73 (24), 5796–5804. DOI: 10.1021/ac0106501.

(43) Hagsten, C.; Innings, F.; Trägårdh, C.; Hamberg, L.; Paulsson, M.; Nylander, T. Removal of UHT Dairy Fouling — An Efficient Cleaning Process by Optimizing the Rate Controlling Alkaline Cleaning Step. *Food Bioprod. Process*. **2019**, 113, 101–107. DOI: 10.1016/j.fbp.2018.11.010.

(44) Noble, P. T. Modeling Transport Processes in Sterilization-in-Place. *Biotechnol. Prog.* **1992**, 8 (4), 275–284. DOI: 10.1021/bp00016a003.

(45) Wang, D.; Mousavi, P.; Hauser, P. J.; Oxenham, W.; Grant, C. S. Quartz Crystal Microbalance in Elevated Temperature Viscous Liquids: Temperature Effect Compensation and Lubricant Degradation Monitoring. *Colloids Surfaces A Physicochem. Eng. Asp*. **2005**, 268 (1–3), 30–39. DOI: 10.1016/j.colsurfa.2005.05.075.

(46) Mercadé-Prieto, R.; Chen, X. D. Dissolution of Whey Protein Concentrate Gels in Alkali. *AIChE J.* **2006**, 52 (2), 792–803. DOI: 10.1002/aic.10639.

(47) Mercadé-Prieto, R.; Paterson, W. R.; Wilson, D. I. The PH Threshold in the Dissolution of β-Lactoglobulin Gels and Aggregates in Alkali. *Biomacromolecules* **2007**, 8 (4), 1162–1170. DOI: 10.1021/ bm061100l.

(48) Fan, L.; Ge, A.; Chen, X. D.; Mercadé-Prieto, R. The Role of Non-Covalent Interactions in the Alkaline Dissolution of Heat-Set Whey Protein Hydrogels Made at Gelation PH 2–11. *Food Hydrocoll*. **2019**, 89 (October 2018), 100–110. DOI: 10.1016/j.foodhyd.2018.10.035.

(49) Gillham, C. R.; Fryer, P. J.; Hasting, A. P. M.; Wilson, D. I. Cleaning-in-Place of Whey Protein Fouling Deposits. *Food Bioprod. Process*. **1999**, 77 (2), 127–136. DOI: 10.1205/096030899532420.

(50) Mercadé-Prieto, R.; Wilson, D. I.; Paterson, W. R. Effect of the NaOH Concentration and Temperature on the Dissolution Mechanisms of Beta-Lactoglobulin Gels in Alkali. *Int. J. Food Eng*. **2008**, 4 (5). DOI: 10.2202/1556-3758.1421.

(51) Saikhwan, P.; Mercadé-Prieto, R.; Chew, Y. M. J.; Gunasekaran, S.; Paterson, W. R.; Wilson, D. I. Swelling and Dissolution in Cleaning of Whey Protein Gels. *Food Bioprod. Process*. **2010**, 88 (4), 375–383. DOI: 10.1016/j.fbp.2010.09.006.

(52) Phinney, D. M.; Feldman, A.; Heldman, D. Modeling High Protein Liquid Beverage Fouling during Pilot Scale Ultra-High Temperature (UHT) Processing. *Food Bioprod. Process*. **2017**, 106, 43–52. DOI: 10.1016/j.fbp.2017.08.007.

(53) Santos, O.; Nylander, T.; Schillén, K.; Paulsson, M.; Trägårdh, C. Effect of Surface and Bulk Solution Properties on the Adsorption of Whey Protein onto Steel Surfaces at High Temperature. *J. Food Eng*. **2006**, 73 (2), 174–189. DOI: 10.1016/j.jfoodeng.2005.01.018.

(54) Santos, O.; Nylander, T.; Paulsson, M.; Trägårdh, C. Whey Protein Adsorption onto Steel Surfaces-Effect of Temperature, Flow Rate, Residence Time and Aggregation. *J. Food Eng*. **2006**, 74 (4), 468–483. DOI: 10.1016/j.jfoodeng.2005.03.037.

(55) Fickak, A.; Al-Raisi, A.; Chen, X. D. Effect of Whey Protein Concentration on the Fouling and Cleaning of a Heat Transfer Surface. *J. Food Eng*. **2011**, 104 (3), 323–331. DOI: 10.1016/j.jfoodeng.2010.11.004.

(56) Hagsten, C.; Altskär, A.; Gustafsson, S.; Lorén, N.; Hamberg, L.; Innings, F.; Paulsson, M.; Nylander, T. Composition and Structure of High Temperature Dairy Fouling. *Food Struct*. **2016**, 7, 13–20. DOI: 10.1016/j.foostr.2015.12.002.

(57) Dolatshahi-Pirouz, A.; Jensen, T.; Foss, M.; Chevallier, J.; Besenbacher, F. Enhanced Surface Activation of Fibronectin upon Adsorption on Hydroxyapatite. *Langmuir* **2009**, 25 (5), 2971–2978. DOI: 10.1021/la803142u.

(58) Rosmaninho, R.; Melo, L. F. The Effect of Citrate on Calcium Phosphate Deposition from Simulated Milk Ultrafiltrate (SMUF) Solution. *J. Food Eng*. **2006**, 73 (4), 379–387. DOI: 10.1016/j.jfoodeng.2005.02.017.

(59) Edvardsson, M.; Rodahl, M.; Kasemo, B.; Höök, F. A Dual-Frequency QCM-D Setup Operating at Elevated Oscillation Amplitudes. *Anal. Chem*. **2005**, 77 (15), 4918–4926. DOI: 10.1021/ac050116j.

(60) Rodahl, M.; Kasemo, B. Frequency and Dissipation-Factor Responses to Localized Liquid Deposits on a QCM Electrode. *Sensors Actuators, B Chem*. **1996**, 37 (1–2), 111–116. DOI: 10.1016/S0925-4005(97)80077-9.

(61) Mersmann, A. Crystallization and Precipitation. *Chem. Eng. Process. Process Intensif.* 1999, 38 (4–6), 345–353. DOI: 10.1016/S0255-2701(99)00025-2.

(62) Belmar-Beiny, M. T.; Gotham, S. M.; Paterson, W. R.; Fryer, P. J.; Pritchard, A. M. The Effect of Reynolds Number and Fluid Temperature in Whey Protein Fouling. *J. Food Eng.* **1993**, 19 (2), 119–139. DOI: 10.1016/0260-8774(93)90038-L.

(63) Arfini, M.; Swedlund, P. J.; Hemar, Y.; Mckinnon, I. R. Calcium Phosphates in Ca2+-Fortified Milk: Phase Identification and Quantification by Raman Spectroscopy. *J. Agric. Food Chem*. **2014**, 62, 12223–12228. DOI: 10.1021/jf503602n.

(64) Sauer, G. R.; Zunic, W. B.; Durig, J. R.; Wuthier, R. E. Fourier Transform Raman Spectroscopy of Synthetic and Biological Calcium Phosphates. *Calcif. Tissue Int*. **1994**, 54 (5), 414–420. DOI: 10.1007/BF00305529.

(65) Kazanci, M.; Fratzl, P.; Klaushofer, K.; Paschalis, E. P. Complementary Information on in Vitro Conversion of Amorphous (Precursor) Calcium Phosphate to Hydroxyapatite from Raman Microspectroscopy and Wide-Angle X-Ray Scattering. *Calcif. Tissue Int.* **2006**, 79 (5), 354–359. DOI: 10.1007/s00223-006-0011-9.

(66) De Aza, P. N.; Santos, C.; Pazo, A.; De Aza, S.; Cuscó, R.; Artús, L. Vibrational Properties of Calcium Phosphate Compounds. 1. Raman Spectrum of β-Tricalcium Phosphate. *Chem. Mater.* **1997**, 9 (4), 912–915. DOI: 10.1021/cm960425d.

(67) Lyster, R. L. J. The Composition of Milk Deposits in an Ultra-High-Temperature Plant. *J. Dairy Res*. **1965**, 32 (2), 203–208. DOI: 10.1017/S0022029900018549.

(68) Heughebaert, J. C.; Nancollas, G. H. Kinetics of Crystallization of Octacalcium Phosphate. *J. Phys. Chem.* **1984**, 88 (12), 2478–2481. DOI: 10.1021/j150656a012.

(69) De Aza, P. N.; Santos, C.; Pazo, A.; De Aza, S.; Cuscó, R.; Artús, L. Vibrational Properties of Calcium Phosphate Compounds. 2. Comparison between Hydroxyapatite and β-Tricalcium Phosphate. *Chem. Mater*. **1997**, 9 (4), 912–915. DOI: 10.1021/cm9604266.

(70) Blanpain-Avet, P.; Hédoux, A.; Guinet, Y.; Paccou, L.; Petit, J.; Six, T.; Delaplace, G. Analysis by Raman Spectroscopy of the Conformational Structure of Whey Proteins Constituting Fouling Deposits during the Processing in a Heat Exchanger. *J. Food Eng*. **2012**, pp 86–94. DOI: 10.1016/j.jfoodeng.2011.12.005.

(71) Jarvis, R. M.; Blanch, E. W.; Golovanov, A. P.; Screen, J.; Goodacre, R. Quantification of Casein Phosphorylation with Conformational Interpretation Using Raman Spectroscopy. *Analyst* **2007**, 132 (10), 1053–1060. DOI: 10.1039/b702944f.

(72) Jullien, C.; Bénézech, T.; Carpentier, B.; Lebret, V.; Faille, C. Identification of Surface Characteristics Relevant to the Hygienic Status of Stainless Steel for the Food Industry. *J. Food Eng.* **2003**, 56 (1), 77–87. DOI: 10.1016/S0260-8774(02)00150-4.

(73) Rosmaninho, R.; Rocha, F.; Rizzo, G.; Müller-Steinhagen, H.; Melo, L. F. Calcium Phosphate Fouling on TiN-Coated Stainless Steel Surfaces: Role of Ions and Particles. *Chem. Eng. Sci*. **2007**, 62 (14), 3821–3831. DOI: 10.1016/j.ces.2007.04.008.

(74) Adamczyk, Z.; Weroński, P. Application of the DLVO Theory for Particle Deposition Problems. *Adv. Colloid Interface Sci*. ***1999***, 83 (1), 137–226. DOI: 10.1016/S0001-8686(99)00009-3.

FOR TABLE OF CONTENTS USE ONLY